The fate of nitrogen in deep magma oceans

Ekanshu Mallick[a,*], Kelsey Prissel[b], Kevin Righter[c], Colin RM Jackson[a]

[a] *Department of Earth and Environmental Sciences, Tulane University, United States*

[b] *Department of Earth, Atmospheric. and Planetary Sciences, Purdue University, United States*

[c] *Department of Earth and environmental Sciences, University of Rochester, United States*

* Corresponding author at: Tulane University, 101 Blessey Hall, New Orleans, LA 70118, United States.

Email address: emallick@tulane.edu (Ekanshu Mallick)

The fate of nitrogen in deep magma oceans

Ekanshu Mallick[a],*, Kelsey Prissel[b], Kevin Righter[c], Colin RM Jackson[a]

[a] *Department of Earth and Environmental Sciences, Tulane University, United States*

[b] *Department of Earth, Atmospheric. and Planetary Sciences, Purdue University, United States*

[c] *Department of Earth and environmental Sciences, University of Rochester, United States*

* Corresponding author at: Tulane University, 101 Blessey Hall, New Orleans, LA 70118, United States.

Email address: emallick@tulane.edu (Ekanshu Mallick)

ABSTRACT

Nitrogen is important in planetary evolution because it is essential to life and the most abundant element in Earth's atmosphere. Here, we investigate how core formation affects the distribution of N within accreting terrestrial planets. We conducted laser-heated diamond anvil cell experiments (LH-DAC) over a wide range of high pressure-temperature-compositional (PTX) conditions (38-103 GPa, 2728-5609 K, -1.95 to -1.03 ΔIW, 0.5-3.7 NBO/T) to study nitrogen partitioning in metal-silicate systems. Combining our data with existing low and high PT results, we developed a nitrogen partitioning model applicable from early accretion to extreme PT stages associated with giant impacts. We test the robustness of our model by accurately predicting nitrogen partitioning in a multi-anvil experiment conducted independently at 15 GPa, 2573 K with oxygen fugacity of -2.5 ΔIW. Our model shows that increasing pressure, oxygen fugacity, and N concentration in the alloy make nitrogen more siderophile, while increasing temperature, oxygen and silicon contents in the alloy, and the SiO_2 content of the silicate melt make nitrogen less siderophile. Application of our model to core formation conditions under oxidized and reduced scenarios suggest that nitrogen can be siderophile or lithophile under low PT conditions but exhibits a neutral partitioning at high PT conditions (> 100 GPa, 5000 K) over a wide range of bulk planet compositions. Using our model, along with partitioning models for S and C, we examine how core formation scenarios can fractionate C/N and S/N ratios in the BSE. Our model suggests that backreaction of volatile rich cores from reduced, smaller impactors (sub-Mars-sized) within deep magma oceans can impart a wide range of C/N and S/N ratios on the magma ocean. We find that the amount of silicate entrainment has a strong control on elemental fractionations imparted to the magma oceans. Elevated C/N and S/N ratios are associated with larger degrees of silicate entrainment, and vice versa. Thus, Earth's apparent depletion of N may relate to its volatiles being reprocessed within deep magma oceans, possibly during the end stages of accretion.

Keywords: Nitrogen, Metal-silicate partitioning, Core Formation, Magma Ocean, Volatiles, LH-DAC

1. Introduction

Nitrogen, being the most abundant element in the atmosphere, plays a pivotal role in Earth's life-forming processes and is paramount in sustaining habitability on the planet. Understanding the distribution and abundance of nitrogen within the planet involves delving into its accretionary history, where planetary-scale processes like core formation and atmospheric evolution have influenced the planet's chemistry. As a volatile siderophile element (VSE), the geochemical behavior of nitrogen strongly impacts its distribution during these accretionary stages.

Earth accumulated its mass through numerous impacts that generated global or partial magma ocean (MO) environments. These MO environments facilitate reactions that set the abundance and distribution of different elements, including nitrogen within the planet (Elkins-Tanton, 2012; Tonks and Melosh, 1993; Wetherill, 1985). Magma ocean production in early accretionary stages may have been facilitated by radiogenic heating, but later stages of magma ocean production were likely driven by impacts from differentiated planetary bodies. Towards the terminal stages of its accretion, production of global and deep magma oceans were driven by giant impacts, with pressures exceeding 100 GPa and temperatures over 6000 K (Canup and Asphaug, 2001; Tonks and Melosh, 1993), and redistribute elements within global planetary reservoirs.

Magma oceans are instrumental in creating compositional differentiation across the different accretionary stages, from planetesimals to protoplanets (Davies, 1985; Halliday et al., 2001; Lee et al., 1976; Tonks and Melosh, 1993; Urey, 1955). During impacts that produce MO environments in protoplanets, the disrupted cores of the differentiated impactors smear through the MO before eventually merging with the proto-core (e.g. Dahl and Stevenson, 2010). Fluid dynamic studies show that the disrupted core emulsifies to different degrees and descends through the magma ocean while entraining different amounts of silicate mass from the magma ocean (e.g. Deguen et al., 2014). This allows for continuous backreaction of the disrupted core with the entrained silicate mass of the larger body which can redistribute elements between the MO and the reacting metal based on their relative siderophilities. Additionally, the MO interacts with the evolving atmosphere, which terrestrial planets like Earth could acquire during their accretion. This MO-atmosphere interaction allows for the redistribution of elements between these two reservoirs based on their volatile natures, influenced by processes like magma ocean degassing and atmospheric loss, hydrodynamic outflow, non-thermal loss due to a weak or non-existent magnetosphere, and giant impact driven loss (Genda and Abe, 2003; Lammer et al., 2008; Moynier et al., 2012; Schlichting et al., 2015; Sekiya et al., 1980; Tucker and Mukhopadhyay, 2014). Consequently, the VSE behavior of nitrogen makes its abundance and distribution within a terrestrial planet susceptible to both core-MO and MO-atmosphere interactions.

Observations on the distribution of nitrogen compared to other VSEs (H, C, S) indicates that N is highly depleted relative to H, C, and S, in the bulk silicate Earth (BSE) reservoir when normalized to CI chondrites (Halliday, 2013; Marty, 2012). This depletion could result from core formation, volatile loss associated with atmospheric evolution or early solar system processes (e.g., Bergin et al., 2015). The exact nature of the source, the mechanisms involved and the timing of VSE delivery to the planet remain debated topics (e.g. Albarède, 2009; Braukmüller et al., 2019; Hirschmann, 2016; Holzheid et al., 2000; Marty, 2012; Wang and Becker, 2013). Regardless of these uncertainties, the partitioning of N in MO-core interactions and the associated backreactions is key to understanding how N gets distributed in both the smaller differentiated impactors that likely delivered volatiles as well as in large terrestrial planets like Earth, which experienced core formation up to extreme PT conditions associated with the later giant impact stages.

In this context, there has been significant work towards understanding how nitrogen behaves in metal (core) - silicate (magma ocean) systems that offer insight on the siderophility of nitrogen, particularly at lower PT conditions, typically below 20 GPa (Dalou et al., 2019, 2017; Grewal et al., 2022, 2021, 2019a, 2019b; Jackson et al., 2021; Li et al., 2023, 2016; Roskosz et al., 2013; Shi et al., 2022; Speelmanns et al., 2019). Beyond this pressure range, data are sparse and are primarily derived from two studies using laser heated diamond anvil cells (LH-DAC) to investigate metal-silicate reactions (Huang et al., 2024; Jackson et al., 2021). While these LH-DAC data provide insights into the behavior of nitrogen under high PT conditions, they struggle to independently constrain the effects of pressure-temperature-compositional (PTX) parameters. The inherent covariance of PTX parameters in LH-DAC experiments complicates the interpretation of nitrogen partitioning between metal and silicate. To address this, more independent datasets from LH-DAC experiments covering non-overlapping PTX domains are necessary. Such datasets can help confirm the consistency of PTX parameter effects or isolate the impact of each parameter, thereby improving the accuracy of nitrogen behavior predictions under high and extreme core formation conditions.

Without the ability to confidently predict the siderophility of nitrogen over the full range of pressures, temperatures, and compositions that prevailed during core formation, we cannot know how Earth's accretionary period set the abundance of nitrogen in the mantle which was eventually available to support habitability. Towards this end, we ran high *PT* multi-anvil (MA) and laser heated diamond anvil cell (LH-DAC) experiments to better constrain nitrogen's partitioning during the extreme conditions of core formation. We ran experiments between 15 GPa and 103 GPa with temperatures up to 5600 K and oxygen fugacity ranging between -2.5 to -1 ΔIW to determine the effects of pressure, temperature, oxidation state, and composition on nitrogen's partitioning. We conclude by applying our data to predict VSE fractionations in deep magma oceans.

3. Methods

We designed a series of laser heated diamond anvil cell (LH-DAC) experiments to test the effect of pressure, temperature, silicate and alloy melt composition, and oxygen fugacity of the system on nitrogen partitioning between metal-silicate ($D_N^{m/s}$) (Table 1). Additionally, we ran a multi-anvil (MA) experiment at 15 GPa to test the efficacy of our nitrogen partitioning model based on previously reported high pressure LH-DAC experiments (>20 GPa), low pressure piston cylinder, MA experiments (<20 GPa) and our new experiments. The different experimental setups and their compositional designs are discussed below.

Starting compositions

We utilize a variety of starting compositions to explore the effect of composition (X) on the partitioning of nitrogen. Our nominal silicate composition is adapted from the primitive

MORB chemistry from Hirschmann et al. (1998) (62a, Appendix A). We modify their composition to a relatively high Mg# (0.83 compared to 0.77) and no alkali elements. We make these modifications to enable exploration of compositional effects around a relatively undifferentiated mantle composition (e.g. Green and Ringwood, 1963). The mixture (SAMCF in Fig 2.1) was prepared by mixing oxides of SiO_2, Al_2O_3, FeO, and MgO. FeO was prepared from Fe_2O_3 by reducing it in a gas mixing furnace at 1773 K under QFM oxygen fugacity (fO_2) for 45 minutes. An alumina crucible was used for doing this reduction. CaO was added after decarbonating $CaCO_3$ at ~1073K for 2-3 hours. The mixture was homogenized using mortar and pestle, and ball-milled in an alumina crucible for 30 minutes. Ball-milling led to additional alumina getting added to our starting composition. This contamination was up to 5 wt% as measured using EDS in an alumina free starting composition that was ball-milled for 30 minutes. We accounted for this contamination when making our starting mixture, although the contamination does lead to variations in the alumina content of our experimental melts (discussed later).

Post ball-milling, 25-30 mg of the mixture was then melted in a gas mixing furnace at 1600 K on a rhenium wire loop and at fO_2 equivalent of QFM for 30 minutes. The fO_2 ensured a dominant divalent Fe in the melt to facilitate later equilibration with Fe alloy (O'Neill, 1987). The melt (glass) bead was then embedded in epoxy and evaluated for homogeneity. We used a Hitachi S-3400 SEM and energy dispersive spectroscopic (EDS) analysis to evaluate and validate the homogeneity of synthesized silicate glass and the absence of quench crystals. Additionally, we created silicate compositions for our fo_2 series of experiments (Table 1) by modifying the nominal silicate composition with variable FeO contents (1 and 4 wt%). Finally, we used iron nitride ($Fe_{2-4}N$) for our metallic-alloy composition, and source of N (7.47 wt% nitrogen), in all our experiments.

2.1 Laser heated diamond anvil cell experiments

After preparing our starting compositions, we assembled the diamond anvil cells (DAC) at Tulane University. Figure 1a shows a schematic cross section of the symmetric DAC assembly with a loaded sample (silicate-alloy). We used diamond culet diameters between 400-200 μm to compress our samples over the span of our targeted high pressures. The seats holding the diamonds were made of tungsten carbide on both the piston and cylinder sides. The gasket was prepared by pre-indenting a rhenium (Re) foil to ~25-30 μm. The desired thickness was created by tracking ruby fluorescence during compression (Mao et al., 2008; Shen et al., 2020). We then created the sample chamber by using a micro-laser cutter to drill a cylinder into the pre-indented Re foil such that it aligns centrally with the axes of the diamonds. The fractional diameter of the sample chamber was between 0.33-0.66 of the culet diameters, with the choice depending on the experimental pressure.

The starting materials were then prepared to be loaded into the sample chamber. Preparations involved making discs of starting materials (silicate glass, metallic alloy, MgO powder, silicate+metallic alloy mix) which were then stacked into the sample chamber depending on the stack design (Fig 2). To make the silicate discs, we embedded our silicate glass into epoxy and polished it to a thickness of ~10-15 μm. This thin layer of silicate glass was then laser cut to match the diameter of our sample chamber. For the metallic alloy discs, we compressed $Fe_{2-4}N$ powder using a diamond anvil to ~7-10 μm thickness, and laser cut alloy discs to match the sample chamber diameter. Additionally, MgO discs and discs of the silicate+metallic alloy mix were prepared for our MgO-saturated experiments and are described below. The laser cut discs were then loaded into the sample chambers guided by different designs as explained below.

2.2 Layer designs for experiments

The layer designs in our sample chambers were adapted from our previous LH-DAC studies (Jackson et al., 2021, 2018). We planned two different designs for our experiments, a nominal design (silicate glass-metallic alloy-silicate glass) that was used for the pressure series and a MgO-(silicate+ metallic alloy mix)-MgO design (MgO-saturated experiments) that was run to test the effect of melt composition on $D_N^{m/s}$ (Figure 1b, c). The nominal layer design for our DAC experiments has an iron nitride disc sandwiched between silicate glass discs (Figure 1b). The glass discs provided thermal and chemical insulation of the metal from the diamonds. Besides running our pressure series using this design, we also ran a few experiments with different glass compositions (variable FeO composition) to explore variations in oxygen fugacity of the system (see Table 1 and results). For the MgO-(silicate+alloy)-MgO designs (Figure 1c), we mixed the silicate and the metallic alloy powders in a 2:1 ratio (wt%) and made discs of 10-15 μm thickness. A disc of this mixture is sandwiched between discs of MgO that were prepared by compression to 10-15 μm thickness and were laser cut as well. Often the laser cut MgO discs were not coherent, and their shapes needed modification using a tungsten needle to fit the sample diameter.

To explore the effect of nitrogen concentration on the partitioning of nitrogen, we modified the alloy by mixing different proportions of $Fe_{2-4}N$ and Fe powders. However, such mixtures suffered from a lack of uniform grain size distribution when mixed using the alumina ball-mill and had larger Fe grains that resulted in inefficient heating and failure during experimentation. This prevented us from systematically evaluating the effect of nitrogen concentration on its partitioning in our experiments.

The assembled DACs were heated in a vacuum oven at 393 K for 12-24 hours to remove moisture absorbed by hygroscopic components in the sample chamber. The DACs were then sealed off from moisture by compressing them to ~2-5 GPa.

2.3 Laser heating

The assembled and sealed off DACs were laser heated at GSECARS (13-ID-D beamline, Advanced Photon Source, Argonne National Lab) to react N-bearing metal and silicate under PT conditions highlighted in Table 1. Specific target pressures were reached and monitored using diamond edge Raman measurements (Akahama and Kawamura, 2006; Dobrosavljevic et al., 2023). We recorded the average pressure of the sample chamber and the associated standard deviation after each heating cycle using diamond edge. During each heating cycle, we used the XRD measurements of mineral phases (e.g., Fe, MgO) with known equations of state to estimate pressure (Fig S-2) (Ono et al., 2010; Sha and Cohen, 2010; Wu et al., 2008). Integration of XRD images and visualization was done using the software DIOPTAS (Prescher and Prakapenka, 2015).

We used a focused ~15-20 μm IR laser beam to heat our samples, coupled from both upstream and downstream sides of the DAC. We first annealed each experiment at ~1500-1800 K to lower any existing pressure gradients within the sample chamber and to identify regions that coupled well with the laser. Selected regions were then heated in a new heating cycle. To heat, we manually controlled the power ramp on the upstream (US) and the downstream (DS) side steadily up to ~2000 K while maintaining minimal temperature difference between the two sides. Temperatures were measured from wavelength of the incandescent radiation from heating the sample which was generally between 660-780 nm. Temperature measurements were processed using T-rax (software by C. Prescher; github.com/CPrescher/T-Rax) that allowed for selection of more accurate wavelength windows that best described a grey body fit of the incandescent intensity (Table S-1). Around 2000 K, we rapidly increased power input until melting was achieved. Melting was confirmed by in-situ XRD measurements, which collect diffraction peaks of phases while heating the sample. Melting was also visually confirmed by a sudden increase in the incandescence of the samples. Some experiments displayed flickering incandescence at higher powers. Many hotspots that displayed flickering later had uncontrolled temperature drops and associated heating failures. Such experiments were not included in our dataset. After confirmation of melting, we acquired repeat measurements of the temperature to confirm temperature stability during the molten state of the heating-spot along with their corresponding XRD measurements. Finally, the sample was quenched by cutting off laser power. The high conductivity of diamond was instrumental for rapid heat loss and quenching. Each heating cycle typically lasted several minutes, with the heating-spots maintained at peak or near-peak temperatures for at least 10 seconds (Figure 2).

Experimental temperature estimates provided in Table 1 are the average temperatures of the final melting temperature measurements (before quenching) collected on the upstream and the downstream sides. Note that each temperature measurement collected on either the upstream or the downstream are averages from a series of rapid measurements of the sample incandescence at the time of collection. The uncertainties of the temperature readings in Table 1 are the combined standard deviations of the final series of measurements taken on the upstream and the downstream. The recorded melting temperatures were used to account for thermal pressure (ΔP_{th} = 2.7 MPa/K, from Siebert et al., 2012) which is added to the recorded diamond edge pressure post heating to get the final pressures reported in Table 1.

2.4 DAC sample preparation for microprobe analysis

The DAC samples were then steadily decompressed at Tulane and preparations commenced for their chemical analysis. We first laser cut the Re around sample chambers to separate them from the remaining gasket, creating a disc nearly the diameter of the diamond culet. Marks for orientation were made on the Re portion of the discs and the discs were mounted on a TEM grid using a tungsten needle.

The heated spots (ref. as hot-spot) on these mounted samples were then cut open to expose a cross section that revealed the synthesized phases. This second step was done at LSU by using a focused ion beam (FIB) with a Ga source (Quanta 3D Dual Beam FEG FIB-SEM) and a plasma focused ion beam (PFIB) with a Xe source (Helios G5 CXe Plasma FIB). Both the instruments accelerate focused ions to mill the sample and explore the exposed cross sections. The PFIB was effective in making larger, coarser cuts at a 60 nA, 30 KeV ion beam current. This allowed for faster removal of the un-melted sample region. The Ga-FIB was then used to make smaller but finer cuts at 1-15 nA and 30 KeV ion beam current. The finer cuts allowed for a more careful survey of the phases being exposed when approaching a hot-spot. Exposure of a hot-spot (Figure 3) was confirmed with secondary electron images.

2.5 Multi-anvil experiment

In addition to the DAC experiments, we ran a multi-anvil (MA) experiment at 15 GPa and 2773 K to corroborate our results obtained from LH-DAC experiments. We followed the sample assembly technique outlined in Righter et al. (2020) and ran the experiment in the 880 ton multi-anvil press at JSC using a 10/5 octahedra assembly. For our starting composition, we used the same 2:1 ratio of silicate+metallic alloy mix that was used for our MgO-saturated LH-DAC experiments. Additionally, we added a 1 wt% Si to the metallic alloy ($Fe_{2\text{-}4}N$) to facilitate metal saturation. We loaded this starting composition into a single crystal MgO capsule. The sample was then heated following previously established power-temperature curves for the specific press and the sample assembly that we utilized (Fig S-1). Temperature was monitored using a type C W/Rh thermocouple up to a reading of 2373 K at which the thermocouple signal was lost. Heating of our sample beyond 2373 K to 2773 K was estimated using the resistivity of the heater, output power, and previous temperature calibration experiments on the same instrument. The experiment was held at 2773 K for ~5 minutes and quenched by shutting off power to the sample heating assembly. The quenched sample was later embedded in epoxy and polished using diamond pastes of increasing grit (up to 5000 grit or ~2 um) for microprobe analysis.

2.6 Electron Microprobe Analysis

The exposed phases were analyzed for their silicate and alloy compositions at JSC using a JEOL 8530F Electron Probe Micro Analyzer. All samples were coated with Ir or Pt to facilitate the analysis of C. Prior to coating, each DAC sample was finely polished using a Ga-FIB (Quanta 3D) at low current. This polishing step was taken to remove any contaminants that had potentially accumulated on the surface since their initial milling and to further polish the sample surface. Polishing was completed with a 1 nA, 30 KeV ion beam. Once samples were polished and coated, they were loaded into the vacuum chamber of the electron microprobe to limit accumulation of C, O, or H on the sample surfaces prior to their analysis.

Primary standards used for calibration were anorthite (for Al, Ca), San Carlos olivine (for Si, Mg), fayalite (for Fe, Si), stainless steel (for Fe, Ni), Si_3N_4 (for N), Fe_3C (for C), and magnetite (for O). Peak intensities for elements of interest were quantified and were corrected for background X-ray intensity. Background was obtained through linear fitting of background intensity around the peaks of elements. Backgrounds and peak positions for light elements (N, C, O) used to quantify their concentrations are shown in Fig S-3. Count times for nitrogen was 90s at peak position and 60s for background, while that for other elements were 30s and 15s, respectively. We also analyzed the secondary standards, including volcanic glass (VG2), fayalite, San Carlos olivine, hyalophane, diopside, and magnetite. All secondary standards except hyalophane are

Smithsonian microbeam standards. Nitrogen was measured on Hyalophane at 0.11+- 0.02 wt% compared to a value of 0.12 wt% reported by Beran et al. (1992). We also analyzed stainless steel to measure the analytical precision and accuracy for alloy forming elements (C, N, Si). The blank concentration of nitrogen was <0.01 wt% measured on nominally nitrogen free secondary standards magnetite, fayalite, diopside and San Carlos olivine. We then analyzed our samples for SiO_2, Al_2O_3, FeO, MgO, CaO, N, and C in the silicate phases and Si, Al, Fe, Mg, Ca, N, C, and O in the metallic phases. Most analysis used a 10 KeV accelerating voltage and a beam current of 10 nA with a beam diameter of 1 µm for the analysis of both silicate and metal phases. We also used variable beam current (3nA and 5 nA) to confirm that nitrogen was not mobilized with variable beam densities.

3. Results

3.1 Experimental phases stabilized

We ran experiments as a pressure series and a compositional series (Table 1) to understand the effects of PTX on the partitioning of nitrogen between metal-silicate. Although we start with fixed bulk initial silicate and metal compositions within the respective designs (Figure 2b and c), we get a wide variation in the silicate and the metal compositions across our samples post experimentation (Table 1, Figure 3.3). This is likely caused from the small variations introduced to the silicate compositions from alumina contamination during ball milling, the variable PT conditions of our experiment, and the local compositional domain sampled by the laser beam (~15-20 µm).

The experiments with both designs (Figure 2 b and c) had a silicate phase (magma ocean equivalent) and a metallic phase (core) at the center of each hot-spot (Figure 3), but the different designed yielded different textures, mineral phase assemblages surrounding the quenched silicate, and major element chemistries. The MgO-saturated experiments often had a layer of ferropericlase and/or bridgmanite encapsulating the silicate and metal phases (Figure 3a). These experiments had depolymerized silicate melts with NBO/T values between 2.7 – 3.7 and were often associated with relatively coarse quench textures in both the metallic and the silicate phases (Figure 3 a,b). Analysis of nitrogen concentrations in these silicate melts varied between 0.6-0.8 wt%, while the associated metallic domains had higher nitrogen concentrations between 4.7-10 wt%. In comparison, the nominal DAC designs had their metal and silicate phases mantled by a $CaSiO_3$-rich layer, likely davemaoite at the PT conditions of our experiments (Figure 3b, Table 1). These experiments had more polymerized silicate melts with NBO/T ranging between 0.5- 1.1. In addition, a stark difference between the two designs was also reflected in the O and the Si contents of the metallic domain, where the MgO saturated experiments had more O (up to 7 wt%), but the nominal designs had more Si content (up to 9.5 wt%). This gave us a wide range of light element concentrations (O, Si) in our metallic domains over a relatively narrow PT space that enables us to more directly explore the effects of these elements on nitrogen siderophility. Carbon was present in our experiments, likely introduced as a contaminant, with up to 5.79 wt% in the metal, after removing blank concentrations of ~0.02 wt% measured on stainless steel.

The multi-anvil experiment (Figure 4) was MgO-saturated and displayed prominent quench textures with metallic blobs (<1 µm to 100s of µm in diameter) amidst the silicate mass. The relative coarse quench texture likely reflects the slower quench and relatively depolymerized composition of this experiment with an NBO/T value of 2.67. The silicate had elongated crystals of MgO and(Mg,Ca) SiO_3 as seen in previously run MgO-saturated MA experiments (e.g., Righter et al., 2020). Although we analyzed silicate domains that had relatively fine crystals, the major element concentrations (in wt%) of FeO, CaO and Al_2O_3 had higher standard deviations (>0.5 wt%) than that found in secondary standards (<0.4 wt%). The MgO and the SiO_2 contents (wt%) across the silicate phase had the most variation with standard deviations 3.5 wt% and 1.8 wt%, respectively which was likely due to sampling of different proportions of quench crystals. Nitrogen and carbon had a similar standard deviation (0.17 wt% and 0.26 wt%, respectively) across the silicate domain as found in the secondary standards (up to 0.14 wt% and 0.20 wt%, respectively). The average nitrogen concentration across the silicate domain was 0.31 wt%. For the metallic analysis, we measured blobs that were between 5-100 µm in diameter (Figure 4). The metal analysis showed more consistent concentrations of elements across the blobs with a maximum standard deviation of 0.42 wt% for the Fe concentration. The concentrations of Si, Al, Mg, and Ca were <0.1 wt%, while the average nitrogen concentration in the metal 10.23 wt% with a standard deviation of 0.41 wt%. The measured oxygen concentration was below the blank concentration of 0.43 wt% measured on stainless steel.

3.2 PTX space explored by our new high-pressure data

We conducted successful experiments that investigated nitrogen partitioning between metal and silicate under previously unexplored PTX conditions (Figure. 5). It is important to note that PTX variables co-vary in our experiments, and any observed trends in Figure 5 are likely influenced by these interdependencies. Our new high-pressure data spans a range of 15-103 GPa, similar to a recent study by Huang et al. (2024). However, our experiments achieved metal-silicate equilibrium over a broader temperature range and higher temperature (2573-6466 K, Figure 5a).

Oxygen fugacity in our experiments showed variations of 1.5 log units with respect to the IW oxygen buffer (calculation described below, Figure. 5b). This range is likely influenced by the experimental temperature and the varying abundance of oxidized and reduced compounds in the laser-heated region, some of which may be contaminants (e.g., H_2O, organic carbon, FeO, Fe). Our experiments produced a diverse range of silicate melts (Figure 5c), enabling us to investigate the effect of silicate melt chemistry on nitrogen partitioning.

The metallic domains synthesized under these high PT conditions allowed for greater incorporation of light elements (Si, O) into the alloy than previously explored (Figures 6a, b; 5d, e). Additionally, our metallic chemistry also captured higher than previously explored nitrogen concentrations (Fig 5f) likely due to nitrogen added as $Fe_{2-4}N$ in our starting composition.

3.3 Determination of oxygen fugacity

Oxygen fugacity of our LH_DAC experiments span between ΔIW-1.03±0.02 and ΔIW-2.51±0.06 and was estimated using the equation below, where ΔIW represents fO_2 calculated as log unit deviation from IW oxygen buffer.

$$\Delta \mathrm{IW} = 2\log\left(\frac{X_{FeO}^{silicate}\gamma_{FeO}^{silicate}}{X_{Fe}^{metal}\gamma_{Fe}^{metal}}\right)$$

The mole fractions of FeO and Fe are determined from analysis. We assume a γ-FeO of 1.25, similar to what was reported by O'Neill and Eggins, (2002) for a MORB system. This assumption is used for our own data and the literature data when computing ΔIW and parameterizing for $D_N^{m/s}$ values below. The γ-Fe of our metallic alloy was evaluated using the Ma, (2001) formalism. This approach enables the application of interaction coefficients for alloying elements (Si, C, S, O) in predicting the non-ideality of Fe in Fe alloy. We use the interaction parameters (ε) for Si-Si, C-C, S-S, O-O, Si-C, Si-O, Si-S, C-O,C-S and O-S interactions from Badro et al. (2018). The equation below shows how γ-Fe is calculated for a N component metallic solution with Fe as the solvent and N-1 solutes (Si, C, S, O).

$$\begin{aligned}
\ln\gamma_{Fe} = {} & \sum_{i=1}^{N-1}\varepsilon_i^i\left(X_i + ln(1-X_i)\right) - \sum_{i=1}^{N-2}\sum_{j=i+1}^{N-1}\varepsilon_i^j X_i X_j\left(1+\frac{\ln(1-X_i)}{X_i}+\frac{\ln(1-X_j)}{X_j}\right) \\
& + \sum_{i=1}^{N-1}\sum_{\substack{j=1\\(j\neq i)}}^{N-1}\varepsilon_i^j X_i X_j\left(1+\frac{\ln(1-X_j)}{X_j}-\frac{1}{(1-X_i)}\right) \\
& + \frac{1}{2}\sum_{i=1}^{N-2}\sum_{j=1+1}^{N-1}\varepsilon_i^j X_i^2 X_j^2\left(\frac{1}{1-X_i}+\frac{1}{1-X_j}-1\right) \\
& - \sum_{i=1}^{N-1}\sum_{\substack{j=1\\(j\neq i)}}^{N-1}\varepsilon_i^j X_i^2 X_j^2\left(\frac{1}{1-X_i}+\frac{1}{1-X_j}+\frac{\mathrm{X}_i}{2(1-X_i)^2}-1\right)
\end{aligned}$$

3.4 Equilibrium check

We evaluate equilibrium in our experiments by **A)** comparing the distributions of Si, O, and Mg in our experiments with literature predictions, **B)** evaluating the spatial variation of major and minor element compositions across metal and silicate domains, and **C)** evaluating the characteristic diffusion length scales of elements in our experiments.

A) We explore the distribution of Si, O, and Mg in our metal-silicate experiments which have been well characterized up to high PT conditions (Badro et al., 2018; Fischer et al., 2015). Strong temperature dependency has been observed in the exchange coefficients of Si and the equilibrium constant associated with the dissociation of MgO (Badro et al., 2018; Fischer et al., 2015), while O has been suggested to exhibit both pressure and temperature dependencies on its metal-silicate partitioning (Fischer et al., 2015). Comparing the distribution of these elements in our experiments with predictions from the literature allowed for the evaluation of the accuracy of our chemical analysis and temperature determinations.

KD-Si (exchange coefficient for Si and Fe between metal and silicate) was determined given the following reaction: SiO_2 (silicate)+ 2Fe (metal) = 2FeO (silicate)+ Si (metal). Without any compositional recalculations (Figure 6a inset), our data have a similar temperature dependency compared to the Fischer et al. (2015) model prediction but generally scatter below the model slope. We recalculate raw (no recalculation) KD-Si values considering Si-O and Si-C interactions using ε parameters from Fischer et al. (2015) and Steelmaking Sourcebook (1988), respectively. The recalculated KD-Si values have small deviations from the raw values (Figure 6a main). Note that our comparison in Figure 6a does not account for the effect of Si-N interactions, and this effect is discussed below. The general scatter below the model prediction is consistent with Si repelling N in Fe alloy.

Values of KD-O were computed based on the dissociation reaction: FeO (silicate) = Fe (metal) + O (metal). Compositionally recalculated values are plotted in Figure 6b (main), while raw KD-O values are plotted in the inset, (Figure 6b inset). Our KD-O values are correlated with temperature, with higher temperature being associated with higher KD-O values, but our data do tend to plot below the isobars associated with our experimental pressures for both recalculated and raw data. Compositional recalculation of KD-O values account for O-Si, O-C, and O-O interactions using the ε parameters from Fischer et al. (2015) and Badro et al. (2015). As with Si, our comparison of KD-O values does not account for the effect of O-N interactions. The general scatter below the model prediction is consistent with O repelling N in Fe alloy, as discussed below.

We also compared the KD-Mg in our experiments with model predictions from Badro et al. (2018). We determined KD-Mg based on the MgO dissociation reaction, where MgO (silicate) = Mg (metal) + O (metal). Values of KD-Mg were recalculated for Mg-O, Mg-Si and Mg-C interactions using ε parameters from the same work. There is good agreement of our recalculated KD-Mg values with the model slope (Figure 6c). One exception is N49-2 for which both the calculated exchange coefficients of Si and the equilibrium constant for the dissociation of MgO suggest colder temperatures than what we determined, scattering beyond the reminder of the data. This sample was therefore rejected from the dataset used for parameterizing $D_N^{m/s}$ values. Taken together, our evaluations of Si, O, and Mg distributions in our experiments suggest that major element exchange between the metallic and silicate domains was efficient at our estimated temperatures and closely approach equilibrium conditions.

B) Another line of evidence for a close approach to equilibrium comes from the evaluation of compositional variation across the metal and the silicate domains in our experiments (Figure 7) using WDS and EDS (Figure 3). Under equilibrium conditions, there should be uniform compositions of the different phases in the assembly at a fixed PTX. Using WDS, we see variability between individual analysis of any given phase beyond the analytical precision of the microprobe (Figure 7). This is likely due to sampling of quenched crystals by the electron beam within respective silcate and metallic domains. Quench crystals tend to form in both our experimental designs, with more depolymerized designs having coarser quench crystals. However, the average concentration of an element measured from multiple analysis across any given phase likely approaches the true chemistry of the phase. This is reflected in the equilibrium distribution of Si, Mg, and O between the metallic and the silicate domains as discussed above (Figure 6). However, there is not any systematic variation of composition across the overall domains that would indicate disequilibrium conditions.

C) We calcuate the characteristic diffusion length scales for major elements in our metallic and silicate domains as a final evalution for the approach to equilibrium in our experiments. Each experiment starts with unreacted materials that must exchange chemistry at high PT conditions to approach equilbrium over the heating duration. We calcuate the diffusion lengthscale using $L = 2\sqrt{Dt}$, where D is the diffusion coefficient of an element and t is time. The large majority of our experiments were conducted above 4000 K and below 100 GPa, and within this PT window the diffusion coefficients of Mg, Si, and O are all found to be near 10^{-9} m^2/s or faster (Karki et al., 2010). Heating durations for our experiments varied but were always greater than 10s (Figure 2). The implied minimium difffusion length scale is 63 µm in silicate. Similarly, diffusion coefficients for liquid Fe alloy are estimated to be 10^{-7} m^2/s or larger for the PT conditions of our experiments (Huang and Badro, 2018). The implied minimum diffusion lengthscale for major elements in our alloy is 200 µm. In comparison the dimensions of our silicate and melt phases (~5-20 um) are always smaller than our calcuated diffusion lengthscales, and this suggests that heating durations of our experiments were sufficently long enough for metal and silicate domains to exchange elements and approach equilbrium.

4. Discussion

4.1 Theoretical basis for parameterization of $D_N^{m/s}$

As established above, our dataset has expanded the PTX coverage of existing data for $D_N^{m/s}$ values, and this permits the parameterization of these data to describe how $D_N^{m/s}$ values vary in response to changes in intensive thermodynamic properties. Towards this end, we first assume that nitrogen in the silicate exists as N^{3-} as suggested by Libourel et al. (2003) for systems more reducing than IW and partitions as neutral N into the metal following the reaction below:

$$(N^{3-})^s + \frac{3}{4}O_2 = N^m + \frac{3}{2}O^{2-} \qquad \text{(Reaction 1)}$$

The equilibrium constant for this reaction can be written as:

$$K_N = \frac{(\gamma_N^m\, X_N^m)(aO^{2-})^{\frac{3}{2}}}{(\gamma_{N^{3-}}^s X_{N^{3-}}^s)(fO_2)^{\frac{3}{4}}} = \frac{(\gamma_N^m)(aO^{2-})^{\frac{3}{2}}}{(\gamma_{N^{3-}}^s)(fO_2)^{\frac{3}{4}}}\, D_N^{\frac{m}{s}} \text{ , or}$$

$$\ln K_N = \ln \gamma_N^m - \ln \gamma_{N^{3-}}^s + \ln D_N^{\frac{m}{s}} - \frac{3}{4}\ln(fO_2) + \frac{3}{2}\ln(aO^{2-}) \qquad \text{(eq 1)}$$

where X_N^m and $X_{N^{3-}}^s$ are mole fractions of nitrogen in the metal and silicate respectively and γ_N^m and $\gamma_{N^{3-}}^s$ are the corresponding activity coefficients. $D_N^{\frac{m}{s}}$ is the partition coefficient of nitrogen between metal and silicate and is expressed as $D_N^{\frac{m}{s}} = \frac{X_N^m}{X_{N^{3-}}^s}$. fO_2 is the oxygen fugacity of the system. We assume the activity of oxygen anion (aO^{2-}) in the silicate melt to be a constant.

By definition, equilibrium constant can be written as:

$$-K_N = \exp\left(\frac{\Delta H^o}{RT} - \frac{\Delta S^o}{R} + \frac{P\Delta V^o}{RT}\right) \qquad \text{(eq 2)}$$

Here, K_N is the equilibrium constant of reaction 1, ΔH^o, ΔS^o, and ΔV^o are the standard enthalpy change, entropy change and volume change of the reaction, R is the gas constant in J/mole/K, and T is temperature in K.

From Eq 1 and Eq 2 and with an assumption that ΔH^o, ΔS^o, and ΔV^o are constant across changes in P and T, $D_N^{\frac{m}{s}}$ can be re-cast as:

$$\ln D_N^{\frac{m}{s}} = a\frac{1}{T} + b\frac{P}{T} + c + \frac{3}{4} ln\,(fO_2) - \ln \gamma_N^m + \ln \gamma_{N^{3-}}^s \qquad \text{(eq 3)}$$

γ_N^m can be computed using the Ma (2001) approach for a ‘N’ component system with Fe as the solvent and ‘n-1’ solutes:

$$\ln \gamma_N^m = ln\,\gamma_{Fe}^m + ln\,\gamma_N^o - \frac{T_{ref}}{T}\varepsilon_N^N \ln(1 - X_N) - \sum_{\substack{j=1 \\ (j\neq N)}}^{n-1} \varepsilon_N^j X_j^{m'} \qquad \text{(eq 4)}$$

Where γ_N^o represents the activity coefficient of nitrogen in the metal at infinite dilution, ε_N^N is the nitrogen self-interaction parameter and ε_N^j is the interaction parameter for the elements j = C, S, Ni, O or Si influencing nitrogen activity in the metal. T_{ref} = 1873 K, the reference temperature at which most steelmaking ε values are reported. $X_j^{m'}$ takes the form:

$$X_j^{m'} = \frac{T_{ref}}{T}\left[\sum_{\substack{j=1 \\ (j\neq i)}}^{n-1} \varepsilon_i^j X_j \left(1 + \frac{\ln(1-X_j)}{X_j} - \frac{1}{(1-X_i)}\right) - \sum_{\substack{j=1 \\ (j\neq i)}}^{n-1} \varepsilon_i^j X_j^2 X_i \left(\frac{1}{1-X_i} + \frac{1}{1-X_j} + \frac{X_i}{2(1-X_i)^2} - 1\right)\right] \qquad \text{(eq 5)}$$

where $X_{i,j}$ are mole fractions of the different elements in the alloy.

We assume $\gamma_{N^{3-}}^s$ follows a symmetric regular solution model (e.g. Ghiorso and Carmichael, 1980):

$$\ln \gamma_{N^{3-}}^s = \frac{\omega_N^i (X_i)^2}{RT} \qquad \text{(eq 6)}$$

for a binary N^{-3} - i solution where i is a silicate melt component and X_i represents the mole fraction of this component other than N^{3-}. ω_N^i is the regular solution parameter for this interaction, R is the gas constant in J/mole/K, and T is temperature in K.

4.2 Model formulation:

Eq 3 gives us the functional forms of PTX parameters that can explain the partitioning of nitrogen between metal and silicate. We then compiled a global dataset (Dalou et al., 2019, 2017; Grewal et al., 2022, 2021, 2019a, 2019c; Huang et al., 2024; Jackson et al., 2021; Li et al., 2023, 2016; Roskosz et al., 2013; Shi et al., 2022; Speelmanns et al., 2019) to parameterize $D_N^{m/s}$ over a wider span of PTX conditions than what our study alone enables. For the Roskosz et al. (2013)

dataset we assume zero carbon concentrations for the LH-DAC data and assume the deviation of the totals from 100% as carbon concentrations for the MA experiments. Additionally, we do not include 7 data points from Grewal et al. (2019a) (discussed in Fig S-4) and one experiment *PC_N_EXP3* from Jackson et al. (2021) with high Si (~13 wt%) in the metal at 0.95 GPa and 1973 K.

Since the alloy effects for N-C, N-S and N-Ni interactions have been systematically studied in earlier works (e.g., Grewal et al., 2019a, 2019b; Jackson et al., 2021; Roskosz et al., 2013; Shi et al., 2022), we recalculate the measured $D_N^{m/s}$ values of our global data for these interactions. It is also necessary to recalculate for these effects considering the absence of these elements in some experimental studies that we include in our global database and their overall subtle effect on the global dataset. To recalculate, we subtract the term $\varepsilon_N^j X_j^{m'}$ from the measured $D_N^{m/s}$ (log) using Eq 5 for C, S, and Ni and the interaction parameters from Jackson et al. (2021).

The C-, S-, Ni- recalculated D_N values were then fit against the other relevant parameters based on Eq 3 using a least squares approach. We evaluate the parameters based on their significance (p-value). The threshold for p-values was set at 0.05, and we did not consider parameters with >0.05 p-values. We started a model with 1/T, P/T and fO_2 as our initial set of parameters based on the thermodynamic rationale presented in Eq 3. Oxygen fugacity, expressed as ΔIW, had the lowest p-value (<0.0001) and gave an R^2 of 0.62 alone. 1/T followed as the subsequent significant term with a p-value <0.0001and increased the R^2 to 0.73. Bringing in the P/T term, however, had a high p-value (>0.05) and was not considered initially for the model.

We then explored the significance of different compositional parameters and their effect on the model fit. For the alloy chemistry effects, we explored the parameters $\ln(1 - X_N)\frac{T_{ref}}{T}$(annotated as $X_N^{m'}$), $X_O^{m'}, X_{Si}^{m'}$, $X_{Mg}^{m}{}', X_{Ca}^{m}{}'$, and $X_{Al}^{m'}$ to identify the alloy solute components that affect $D_N^{\frac{m}{s}}$. The $X_j{}'$ values (j = N, O, Si, Mg, Ca, Al) were calculated using Eq 5. The terms $X_{Si}^{m'}$ and $X_N^{m'}$ had the highest significance with p-values <0.0001 followed $X_O^{m'}$with a p-value of 0.01. $X_{Mg}^{m}{}', X_{Ca}^{m}{}'$ and $X_{Al}^{m'}$ had p-values >0.05 and were not included in the model. The overall model had an R^2 of 0.78 at this step.

We evaluated the significance of our oxide parameters (i=SiO_2, Al_2O_3, MgO and CaO) in their functional form $\frac{\omega_N^i (X_i)^2}{RT}$. We did not fit for FeO given its direct correlation with the ΔIW term, already included in the model. Amongst our oxide parameters, we found that SiO_2 and MgO have higher significance (p-values <0.0001) than CaO and Al_2O_3. The SiO_2 and the MgO contents are anticorrelated in the experiments and can therefore be used interchangeably to capture the effect of silicate composition on N. However, choosing either SiO_2 or MgO as the first significant silicate parameter had implications on the next choice of silicate parameters and on the slope of the already identified significant parameters. Choosing MgO as the first silicate parameter, CaO and Al_2O_3 followed suit as the next silicate parameters. Each of these terms (MgO, CaO, Al_2O_3) had positive coefficients, which suggested that their enrichment in the melt makes nitrogen more siderophile.

With this choice of silicate parameters, SiO_2 became less significant with a p-value of 0.0206. The model R^2 value was 0.87 with this choice.

Choosing SiO_2 as the first silicate parameter, on the other hand, yielded a negative coefficient and suggested that nitrogen becomes less siderophile with SiO_2 enrichment in the silicate melt. The R^2 of the model when choosing SiO_2 as the significant silicate parameter was 0.84. Choosing SiO_2 as the silicate parameter decreased the slope of ΔIW from 0.54 to 0.39. This deviation further away from the ¾ slope is expected for a N^{3-} dominated speciation in the silicate melt. Given the choice of MgO or SiO_2 to describe melt compositional effects, we selected SiO_2. Our decision here is driven by evidence for Si-N^{3-} interactions in silicate melts (Huang et al., 2022) that should act to stabilize nitrogen in the silicate and decrease its siderophility (consistent with the negative coefficient we retrieve from our fitting).

Finally, the P/T term became significant with a p-value of 0.0059 after considering the compositional terms discussed above, while the overall model R^2 improved by 0.004. The significance of this term was independent of our choice for the silicate melt parameter.

With the 7 PTX parameters identified from the procedure described above our final model takes the form in Eq 7 with an R^2 of 0.84.

$$\log D_N^{\frac{m}{s}} = \frac{5559.4(\pm 450.6)}{T\,(K)} + \frac{33.3(\pm 12.0)P(GPa)}{T(K)} + 0.39(\pm 0.02)\Delta\mathrm{IW} - 5.46(\pm 1.29)X_N^{m'} +$$

$$8.72(\pm 2.66)\, X_O^{m'} + 9.05(\pm 1.04)X_{Si}^{m'} - 54023(\pm 5055)\left(\frac{{X_{SiO_2}^{S}}^{2}}{R.T(K)}\right) - 0.11(\pm 0.22) \qquad \text{(eq 7)}$$

Note that Eq 7 is derived for systems without C, Ni, and S. To include these compositional effects in predictions we suggest adding interaction terms analogous to those given for oxygen or silicon, although this complicates propagation of uncertainties.

4.3 Model parameters and their implications:

Our model from Eq 7 allows us to understand the behavior of nitrogen during core formation with the most diverse PTX coverage to date (Figure 3). Based on our model fits, we infer that pressure has a positive effect on the siderophility of nitrogen, while temperature has a negative influence on its siderophility (Figure 8a). Our temperature sensitivity is similar to previous determinations (Grewal et al., 2019a; Huang et al., 2024; Jackson et al., 2021; Shi et al., 2022; Speelmanns et al., 2019). Although there is uniform agreement that higher temperatures make N less siderophile, there is more disagreement regarding the role of pressure in modulating nitrogen partitioning. The models presented by Dalou et al. (2017) and Speelmanns et al. (2019) suggest negligible pressure effect between 1.2-3 GPa and 0.85-5.5 GPa, respectively, whereas models by Grewal et al. (2019a, 2019b) (1-6 GPa) and Shi et al. (2022) (1-8 GPa) report a positive effect of pressure on nitrogen's siderophility. Higher pressure behavior of nitrogen beyond 8 GPa was explored by Huang et al. (2024), Jackson et al. (2021) and Roskosz et al. (2013) but these studies had different conclusions on the effect of pressure. While Roskosz et al. (2013) did not observe any conclusive effect of pressure on $D_N^{m/s}$ in their experiments conducted up to ~15 GPa, Jackson et al. (2021) ran experiments between 0.95 -25.6 GPa and their model suggested that pressure increases the siderophility of nitrogen. Although, Huang et al. (2024) did not require any pressure effect in their model that included higher PT data up to 104 GPa. Our conclusion regarding the positive effect of pressure on nitrogen partitioning is enabled by the expanded PTX provided by our dataset.

We find that oxygen fugacity of the system has a positive effect on nitrogen siderophility, meaning more oxidized conditions favor nitrogen siderophility (Figure 8b). This relationship qualitatively consistent with Reaction 1 and is consistent with other nitrogen metal-silicate partitioning studies (Dalou et al., 2019; Grewal et al., 2019a; Huang et al., 2024; Jackson et al., 2021; Li et al., 2016; Shi et al., 2022; Speelmanns et al., 2019). The coefficient we find for ΔIW, however, is 0.39 (±0.02), much lower than the 0.75 slope predicted by Eq 3 for Reaction 1. A large deviation from the 0.75 slope may suggest the involvement of a N_2 species as a solute component in the silicate phase or the stabilization of N^{-3} by Fe^{+2} dissolved in the melt. There is evidence from molecular dynamical work that N^{-3} does complex with Fe^{+2} and Si^{+4} under PT conditions relevant to this study (Huang et al., 2022). Oxidizing and N-rich conditions promote N_2 stability over N^{3-} and could require a different reaction to constrain nitrogen's partitioning, as below.

$$N_2^{silicate} = 2N^{metal} \qquad \text{(Reaction 2)}$$

If N_2 dominates the budget of N in melt then N partitioning would become insensitive to oxygen fugacity (Dasgupta et al., 2022; Libourel et al., 2003; Mysen et al., 2014), lowering the coefficient ΔIW. Thus, there should be a PTX boundary where the Eq 7 is no longer valid. Experiments conducted under low PT conditions (up to 10 GPa and 1773 K) identify the redox boundary between N^{3-} and N_2 dominated melt solubility near IW (Libourel et al., 2003), but it has not been defined for the PTX conditions associated with laser heated DAC studies (this study; Huang et al., 2024). Further systematic investigation of high PTX experiments are needed to find such a redox boundary and to evaluate the accuracy of our model in the N_2 dominated conditions.

Our model also suggests that the Si, O and N contents of the alloy influence the siderophility of nitrogen. We find that Si has a negative effect on nitrogen siderophility (Figure 9a), as suggested by Grewal et al. (2019a), Shi et al. (2022), and Huang et al. (2024a). Although, the magnitude of this interaction determined by Grewal et al. (2019a) is different from that determined by Shi et al. (2022) and Huang et al. (2024a) likely due to differences in the assumed structural form of the parameter in their models. These studies report interaction parameters that do not scale with temperature, which when applied to the extreme temperatures associated with core formation may underestimate the partitioning of nitrogen into the core (overpredict strength of interaction).

Furthermore, the interaction parameter based on our model fit for N-Si interaction (ε_N^{Si}) was 9.06 (±1.05), determined for a reference temperature of 1873 K. Our N-Si interaction coefficient is fit with data that span a wide range of temperatures, and this provides confidence in using the 1/T scaling assumed here for describing non-ideal solution terms. Application of the ε_N^{Si} value in our model to any desired temperature considers temperature scaling of this interaction term as shown in Equations 4 and 5. Considering this ε_N^{Si} value to compositionally recalculate the KD-Si values from Figure 6a, the recalculated KD-Si values shift close to the slope predicted by Fischer et al. (2015) as shown in Figure 10a.

Oxygen has a similar effect on nitrogen as Si, where the incorporation of oxygen into the alloy makes nitrogen less siderophile (Figure 9b). Our finding is qualitatively consistent with the model from Huang et al. (2024) who also report a negative effect of oxygen on nitrogen siderophility. Although, the coefficient reported in their model does not scale with temperature. The interaction parameter for N-O interaction in the metallic alloy (ε_N^{O}) based on our model fit was 8.72 (±2.68), determined for a reference temperature of 1873 K. Application of this term in our model considers temperature scaling like ε_N^{Si} does above. We used this ε_N^{O} value to compositionally recalculate for N-O interaction in Figure 4b. The KD-O data recalculated for N-O interaction shifts up towards the model predictions from Fischer et al. (2015), despite observable differences from the trend predicted by Fischer et al. (2015) (Figure 10b).

In contrast to the effect of Si and O, the negative self-interaction coefficient, ε_N^{N}, of 5.35 (±1.56) suggests more siderophile behavior with increasing the concentration of nitrogen in metal (Figure 9c). Experimental systems tend to have high nitrogen concentrations (Figure 5f), and thus the N-N interaction parameter suggests current data are biased to high $D_N^{m/s}$ values when applying to natural systems with low nitrogen concentrations.

Lastly, our model predicts that the SiO_2 content of the silicate makes nitrogen less siderophile (Figure 9d). The effect of silicate melt has been quantified as NBO/T in previous studies (Grewal et al., 2019a; Huang et al., 2024; Shi et al., 2022), which proxies for the structure of the silicate melt. Although, the melt structure varies with pressure and temperature, as well as composition (e.g. Huang et al., 2022). Nonetheless, there are discrepancies on the effect of NBO/T on nitrogen siderophility. Speelmanns et al. (2019) do not observe any significant effect of the NBO/T within the range of their silicate melt composition (0.1-1.3). Grewal et al. (2019a) model the effect of NBO/T within a range of 0.4-2.5 and report a positive effect on nitrogen siderophility. Shi et al. (2022) observe a similar effect within an NBO/T range of 0.02-3.1, suggestive of a greater siderophile behavior with a more depolymerized melt. This positive correlation is also corroborated by Huang et al. (2024) who explored relatively depolymerized melts with NBO/T ranging between 2.4-3.2. Our experimental designs allow us to explore the effect of silicate melt composition over a wide range of melt polymerization (Figure 11) with the nominal designs having a range of NBO/T between 0.5- 1.1 and the MgO saturated designs between 2.7-3.7. We see a similar correlation with NBO/T in our experiments as Grewal et al. (2019a), Shi et al. (2022) and Huang et al. (2024), where the MgO-saturated experiments tend to witness a greater siderophile behavior of nitrogen than the nominal designs (Figure 11). Though NBO/T correlates with silicate melt composition as a broader term, it does not reflect the chemical interaction that nitrogen has within the melt. Our model captures this chemical interaction with SiO_2 in the melt and suggests that N-Si interaction in the silicate melt makes nitrogen less siderophile (Figure 9d). Although, as discussed above, different silicate melt models yield similar quality of fits to the data, and we favor using SiO_2 given the evidence for Si-N interactions in reduced melts (Huang et al., 2022) and the relatively simple functional form. Lower SiO_2 melts are associated with more siderophile behavior for N, and this is qualitatively consistent with Si-N interactions helping to stabilize N in melt. Additionally, the functional form considers scaling of the symmetric regular solution parameter ω_N^{SiO2} with temperature (Eq 6), unlike NBO/T.

4.4 Model Validation

We used our model from Eq 7 to predict nitrogen partitioning in our multi-anvil experiment. The multi-anvil experiment was run at 15 GPa and 2773 K, a PT location that has relatively sparce data in the global compilation (Figure 8a) and utilizes a method that is distinct from the large majority of experiments used to determine our parameterization. Predicting nitrogen partitioning in this experiment, external to our global compilation, allowed us to evaluate the consistency of our model beyond where there is dense PTX coverage. Our model prediction falls within 95% confidence interval of the observed partition coefficient of the MA experiment (Figure 12). The success of our model to predict $D_N^{m/s}$ values in PTX regions with relatively poor data coverage and with distinct methodology provides confidence in applying Eq 7 to natural systems. Adding the MA experiment to the global compilation does not affect parameters values or identify additional significant parameters.

4.5 $D_N^{m/s}$ variations across PTX conditions

With Eq 7 established, we can now better predict the behavior of nitrogen in an accreting proto-Earth. Core formation likely proceeded from early episodes dominated by low PT conditions to later episodes where more extreme PT conditions prevailed (e.g. Canup and Asphaug, 2001; Tonks and Melosh, 1993). We apply our $D_N^{m/s}$ model to core formation scenarios assuming a mantle liquidus from Fiquet et al. (2010) to constrain potential PT conditions of metal-silicate reaction (Fig 13a). We apply the formalism in Rubie et al. (2011) to predict the major element chemistry of metal and silicate reacting over the range of PT conditions considered here and apply their “reduced” and an “oxidized” bulk planet compositions.

Predicted $D_N^{m/s}$ values for a “reduced” protoplanet are less than one (lithophile) across the PT conditions we explore in Figure 13a. Low PT conditions produce a more pronounced lithophile behavior of nitrogen, while $D_N^{m/s}$ values shift marginally higher as PT conditions increase. The overall lithophile behavior of N throughout the PT range in Figure 13a for a reduced protoplanet reflects that the net effect of the rise in Si and O with increase in temperature (forcing $D_N^{m/s}$ down) remain roughly balanced by the rise in the oxygen fugacity (ΔIW) of the system and pressure (forcing $D_N^{m/s}$ up) in a reduced protoplanet system.

Predicted $D_N^{m/s}$ values for an “oxidized” protoplanet decrease by approximately an order of magnitude across the PTX range of conditions associated with these scenarios (Figure 13a). Oxidizing conditions promote higher $D_N^{m/s}$ values under low PT conditions, but as PT conditions increase, the effects of temperature, Si and O content work to drive down $D_N^{m/s}$ values, more than offsetting the effects of pressure and oxygen fugacity. We predict little difference in $D_N^{m/s}$ values above 100 GPa between oxidized and reduced protoplanets.

Upon applying the nitrogen partitioning model from Huang et al. (2024) to the PTX space explored in Figure 13a we observe similar trends of the predicted $D_N^{m/s}$ values across both the "oxidized" and the "reduced" systems (Figure 13b, c), where the siderophility of nitrogen decreases with increasing PT conditions. In both scenarios, their predicted $D_N^{m/s}$ values have smaller differences from our model predictions at low PT but at high PT conditions their predictions suggest an order of magnitude lower siderophility of nitrogen than what our models predict. Note that we assume zero C and S and an NBO/T value of 2.6 to predict $D_N^{m/s}$ using the Huang et al. (2024) model.

4.6 Elemental fractionations of VSEs by core formation

We now apply Eq 7 towards understanding how N and other VSEs are redistributed during terrestrial planet accretion. The concentration of VSEs in BSE shows a general depletion of nitrogen with respect to hydrogen, sulfur and carbon when normalized to CI chondrite (Halliday, 2013; Hirschmann, 2016; Marty, 2012; Wasson et al., 1997). CI chondrites and the Sun are similar in composition and CI chondrites may therefore provide an estimate for the VSE ratios of the bulk solar system (Anders and Grevesse, 1989; Lodders, 2003; Palme et al., 2014). It is clear that many processes can fractionate VSEs as witnessed by the variable VSE ratios of chondrites and varying magmatic solubilities of VSE (e.g., Bergin et al., 2015; Hellmann et al., 2020; Vollstaedt et al., 2020). We focus here on the ability of core formation to induce VSE fractionations on the silicate portions of larger terrestrial bodies such as Earth.

To explore how core formation can induce VSE fractionations we first compare our predicted $D_N^{m/s}$ values with the partition coefficients of other VSEs (C and S) with increasing PT conditions for core-formation in an "oxidized" and a "reduced" system (Figure 13 b, c). We take the exchange coefficient model of carbon from Blanchard et al. (2022) for both possible +2 and +4 valence states of carbon. We also use the Eq 1 from Fischer et al. (2020) to predict $D_C^{m/s}$ which includes the effects of ΔIW, light elements in the alloy (O and S) and NBO/T on carbon partitioning in addition to PT terms. We assume sulfur-free calculations of $D_C^{m/s}$ when using this equation and assume an NBO/T value of 2.6. The partitioning of sulfur ($D_S^{m/s}$) was calculated using Eq S-8 from Jackson et al. (2021) assuming a carbon free system and the activity coefficient of Fe as one. We focus on C/N and S/N ratios because carbon and sulfur are relatively well studied under higher PT conditions compared to H (Blanchard et al., 2022; Dalou et al., 2017; Fischer et al., 2020; Grewal et al., 2019c; Jackson et al., 2021; Tagawa et al., 2021). The predicted C and S partition coefficients are plotted in Figure 13 b and c. C and S remain siderophile across the PTX space of core formation, although they exhibit a lowering of this siderophile tendency with increasing PT conditions. Nitrogen, in comparison, has a lower preference for the metallic alloy across the PTX span regardless of the oxidation state of the system.

We now apply the VSE partition coefficients to a two-stage core formation model. Our model is intended to model how metal-silicate reactions associated with differentiated bodies impacting into a nearly fully grown Earth can fractionate VSE ratios. N-body simulations suggest that this type of interaction was relatively common during the giant impact stage of planetary growth (e.g., Agnor et al., 1999; Canup and Asphaug, 2001; Wetherill, 1985). In the first stage we react metal and silicate of the impactor at 10 GPa and 2500 K for "reduced" and "oxidized" protoplanets to simulate core formation within a smaller protoplanet bodies. We calculate the composition of metal and silicate using the batch equation as follows:

$$[i]_{metal} = \frac{D_i^{m/s} . [i]_{bulk}}{D_i^{m/s} + \left(1 - D_i^{m/s}\right) . f_{silicate}}$$

$$[i]_{silicate} = \frac{[i]_{bulk}}{D_i^{m/s} + \left(1 - D_i^{m/s}\right) . f_{silicate}}$$

Here, [i] is the N, C or S, $D_i^{m/s}$is the partition coefficient of the element and $f_{silicate}$is the mass fraction of the silicate phase that is in equilibrium with the reacting metal. We assume bulk 1 wt % S, 1 wt % C and 100 ppm N (although only N partitioning depends on N concentration) and that the core is 1/3 of the overall protoplanet mass. Note that our model is focused on how VSE are fractionated, rather than predicting absolute concentrations, so the bulk concentrations of C and S are essentially placeholders.

In the second stage we then take the core from the first stage calculation and let it backreact with a deep magma ocean (100 GPa, 5000 K), also exploring "reduced" and "oxidized" protoplanet scenarios to set the VSE partition coefficients for these more extreme conditions. The goal is this step is to calculate the chemical consequences of smaller differentiated body accreting to a nearly Earth-sized differentiated body. We assume the magma ocean of the nearly Earth-sized body is devoid of VSEs before reacting with the core from the first step.

Figure 14a plots predicted C/N and S/N ratios of the magma ocean against the metal/silicate ratio associated with core backreaction (i.e., the second stage) for the "reduced" protoplanet scenario. VSE ratios are normalized to their bulk ratios associated with the first stage calculation. We take the metal/silicate ratio associated with backreaction as a free parameter because it depends on the fluid dynamics of the dense metal falling through the magma ocean, which are still a topic of study (Dahl and Stevenson, 2010; Deguen et al., 2014; Maas et al., 2021; Qaddah et al., 2019). At high metal/silicate ratios in Figure 14a, the predicted C/N and S/N ratios in the silicate phase are relatively low, reflecting that nitrogen is a relatively lithophile VSE near 100 GPa. As metal/silicate ratios decrease (potentially reflecting more silicate entrainment in downwelling metal-rich plumes or less emulsification of the impactor core), the C/N and S/N ratios rise and approach the composition of the impactor core from the first stage calculation (Figure 14a).

Figure 14b plots the predicted C/N and S/N ratios against the metal/silicate ratio associated with core backreaction within a deep magma ocean (second stage) for the "oxidized" protoplanet scenario. In this case, the impactor core from the first step calculation itself has a lower degree of VSE fractionation since nitrogen remains siderophile, although less than C and S, under low PT conditions associated with the first stage. Under deep magma ocean environments in the second step, C/N and S/N ratios in the silicate phase remain less than 1 across almost any assumed metal/silicate ratio, which is a manifestation of the oxidized impactor core having a lower C/N and

S/N ratio from the first stage. As the metal/silicate ratio approaches extreme metal dilution, the C/N and S/N ratios in the silicate phase also approach the impactor core chemistry from the first stage calculation.

Figure 15 illustrates core formation scenarios during the second stage calculation with variable metal/silicate ratios and variable VSE fractionations. Figure 15a shows a scenario of high metal/silicate ratio under which VSE fractionations would produce low C/N and S/N ratios. In contrast, if the metal entrains a larger amount of the magma ocean that it reacts with (Figure 15b), the magma ocean would acquire elevated C/N and S/N ratios due to the metal-silicate interaction.

Taken together, we find that backreaction of cores produced at lower PT conditions within deep magma oceans can induce a wide variety of VSE fractionations (Figure 15). Our modeling highlights the importance of redox conditions that prevailed within smaller differentiated bodies and the metal/silicate ratio associated with the backreaction of impactor cores within deeper (higher PT) magma oceans in modulating VSE ratios. Reduced bodies have a greater potential to produce cores with elevated C/N and S/N ratios compared to oxidized bodies given the partitioning of VSEs under lower PT conditions (Figure 13). The backreaction of cores from impactors within deeper magma oceans offers a second opportunity to fractionate VSEs. Backreaction with a high associated metal/silicate ratio imparts low C/N and S/N ratios given the relative lithophile nature of N compared to other VSEs under more extreme PT conditions (Figure 13), while backreaction with a low associated metal/silicate ratio imparts higher C/N and S/N ratios that approach the initial ratios of the impactor cores. Bulk silicate Earth has elevated C/N and S/N ratios, and given our modeling, this may point to the importance of reduced protoplanets and larger amounts of silicate entrainment during later stages of core formation for setting the volatile budget of Earth.

5. Conclusion

Our study expands the PTX space where the partitioning behavior of nitrogen is constrained, particularly for extreme PT conditions and depolymerized melts. We conducted laser-heated diamond anvil cell experiments and a multi-anvil experiment, spanning pressures from 15 to 103 GPa and temperatures from 2573 to 5609 K, examining silicate melts with a broad range of polymerization (NBO/T: 0.5-3.7). In addition to generating new PTX data, we compiled existing experimental data to parameterize nitrogen partitioning between metal and silicate across a wide range of PTX conditions.

Our model indicates that pressure, oxygen fugacity, and bulk nitrogen concentration of the system make nitrogen more siderophile, while temperature, oxygen and silicon content of the metallic alloy, and the SiO_2 content of the silicate melt makes nitrogen less siderophile.

We apply our model to explore VSE fractionations (C/N and S/N) within smaller differentiated bodies as well as in larger proto-planets due to core formation. Using a two staged core formation model, we find that cores of smaller (moon-Mars sized) “reduced” bodies are effective candidates to impart elevated C/N and S/N ratios to the magma ocean of proto-Earth, during its later stages of core formation. Finally, the amount of magma ocean that the impactor core effectively interacts with during its breakdown and descent can further elevate or lower the elemental ratios.

CRediT authorship contribution statement

Ekanshu Mallick: Writing- Original Draft, Writing - Review & Editing, Conceptualization, Methodology, Investigation, Data curation, Software, Validation, Formal analysis, Visualization. **Kelsey Prissel:** Investigation, Validation, Writing - Review & Editing. **Kevin Righter:** Writing - Review & Editing, Project administration. **Colin RM Jackson:** Conceptualization, Funding acquisition, Project administration, Resources, Supervision, Methodology, Investigation, Validation, Writing -Review & Editing.

Declaration of Competing Interest

The authors declare that they have no known competing financial interests or personal relationships that could have appeared to influence the work in this paper.

Acknowledgements

This project was supported by NASA Emerging Worlds Grant 80NSSC21K0377. We thank Vitali Prakapenka and Stella Chariton for support during the high-pressure experiments conducted at GeoSoilEnviroCARS (The University of Chicago, Sector 13), the Advanced Photon Source, Argonne National Laboratory, and for discussions on temperature determination using T-rax software. We thank Dongmei Cao for assistance with using the focused ion beam at Louisiana State University.

Appendix A. Supplementary materials

The following supplementary materials are included in support of this paper.

Supplementary Tables S-1, S-2, S-3

Supplementary Figures S-1, S-2, S-3, S-4

Data availability

Trax data (.spe) are available through Mendeley data at

https://doi.org/10.17632/2r2b7p6g6m.1

References

Akahama, Y., Kawamura, H., 2006. Pressure calibration of diamond anvil Raman gauge to 310GPa. Journal of Applied Physics 100, 043516. https://doi.org/10.1063/1.2335683

Albarède, F., 2009. Volatile accretion history of the terrestrial planets and dynamic implications.

Anders, E., Grevesse, N., 1989. Abundances of the elements: Meteoritic and solar. Geochimica et Cosmochimica Acta 53, 197–214. https://doi.org/10.1016/0016-7037(89)90286-X

Badro, J., Aubert, J., Hirose, K., Nomura, R., Blanchard, I., Borensztajn, S., Siebert, J., 2018. Magnesium Partitioning Between Earth's Mantle and Core and its Potential to Drive an Early Exsolution Geodynamo. Geophysical Research Letters 45, 13,240-13,248. https://doi.org/10.1029/2018GL080405

Badro, J., Brodholt, J.P., Piet, H., Siebert, J., Ryerson, F.J., 2015. Core formation and core composition from coupled geochemical and geophysical constraints. Proceedings of the National Academy of Sciences 112, 12310–12314. https://doi.org/10.1073/pnas.1505672112

Bergin, E.A., Blake, G.A., Ciesla, F., Hirschmann, M.M., Li, J., 2015. Tracing the ingredients for a habitable earth from interstellar space through planet formation. Proceedings of the National Academy of Sciences 112, 8965–8970. https://doi.org/10.1073/pnas.1500954112

Blanchard, I., Rubie, D.C., Jennings, E.S., Franchi, I.A., Zhao, X., Petitgirard, S., Miyajima, N., Jacobson, S.A., Morbidelli, A., 2022. The metal–silicate partitioning of carbon during Earth's accretion and its distribution in the early solar system. Earth and Planetary Science Letters 580, 117374. https://doi.org/10.1016/j.epsl.2022.117374

Braukmüller, N., Wombacher, F., Funk, C., Münker, C., 2019. Earth's volatile element depletion pattern inherited from a carbonaceous chondrite-like source. Nat. Geosci. 12, 564–568. https://doi.org/10.1038/s41561-019-0375-x

Canup, R.M., Asphaug, E., 2001. Origin of the Moon in a giant impact near the end of the Earth's formation. Nature 412, 708–712. https://doi.org/10.1038/35089010

Dahl, T.W., Stevenson, D.J., 2010. Turbulent mixing of metal and silicate during planet accretion — And interpretation of the Hf–W chronometer. Earth and Planetary Science Letters 295, 177–186. https://doi.org/10.1016/j.epsl.2010.03.038

Dalou, C., Füri, E., Deligny, C., Piani, L., Caumon, M.-C., Laumonier, M., Boulliung, J., Edén, M., 2019. Redox control on nitrogen isotope fractionation during planetary core formation. Proc. Natl. Acad. Sci. U.S.A. 116, 14485–14494. https://doi.org/10.1073/pnas.1820719116

Dalou, C., Hirschmann, M.M., von der Handt, A., Mosenfelder, J., Armstrong, L.S., 2017. Nitrogen and carbon fractionation during core–mantle differentiation at shallow depth. Earth and Planetary Science Letters 458, 141–151. https://doi.org/10.1016/j.epsl.2016.10.026

Dasgupta, R., Falksen, E., Pal, A., Sun, C., 2022. The fate of nitrogen during parent body partial melting and accretion of the inner solar system bodies at reducing conditions. Geochimica et Cosmochimica Acta 336, 291–307. https://doi.org/10.1016/j.gca.2022.09.012

Davies, G.F., 1985. Heat deposition and retention in a solid planet growing by impacts. Icarus 63, 45–68. https://doi.org/10.1016/0019-1035(85)90020-X

Deguen, R., Landeau, M., Olson, P., 2014. Turbulent metal–silicate mixing, fragmentation, and equilibration in magma oceans. Earth and Planetary Science Letters 391, 274–287. https://doi.org/10.1016/j.epsl.2014.02.007

Dobrosavljevic, V.V., Zhang, D., Sturhahn, W., Chariton, S., Prakapenka, V.B., Zhao, J., Toellner, T.S., Pardo, O.S., Jackson, J.M., 2023. Melting and defect transitions in FeO up to pressures of Earth's core-mantle boundary. Nat Commun 14, 7336. https://doi.org/10.1038/s41467-023-43154-w

Elkins-Tanton, L.T., 2012. Magma Oceans in the Inner Solar System. Annual Review of Earth and Planetary Sciences 40, 113–139. https://doi.org/10.1146/annurev-earth-042711-105503

Fiquet, G., Auzende, A.L., Siebert, J., Corgne, A., Bureau, H., Ozawa, H., Garbarino, G., 2010. Melting of Peridotite to 140 Gigapascals. Science 329, 1516–1518. https://doi.org/10.1126/science.1192448

Fischer, R.A., Cottrell, E., Hauri, E., Lee, K.K.M., Le Voyer, M., 2020. The carbon content of Earth and its core. Proceedings of the National Academy of Sciences 117, 8743–8749. https://doi.org/10.1073/pnas.1919930117

Fischer, R.A., Nakajima, Y., Campbell, A.J., Frost, D.J., Harries, D., Langenhorst, F., Miyajima, N., Pollok, K., Rubie, D.C., 2015. High pressure metal–silicate partitioning of Ni, Co, V, Cr, Si, and O. Geochimica et Cosmochimica Acta 167, 177–194. https://doi.org/10.1016/j.gca.2015.06.026

Genda, H., Abe, Y., 2003. Modification of a proto-lunar disk by hydrodynamic escape of silicate vapor. Earth Planet Sp 55, 53–57. https://doi.org/10.1186/BF03352462

Ghiorso, M.S., Carmichael, I.S.E., 1980. A regular solution model for met-aluminous silicate liquids: Applications to geothermometry, immiscibility, and the source regions of basic magmas. Contr. Mineral. and Petrol. 71, 323–342. https://doi.org/10.1007/BF00374706

Green, D.H., Ringwood, A.E., 1963. Mineral assemblages in a model mantle composition. Journal of Geophysical Research (1896-1977) 68, 937–945. https://doi.org/10.1029/JZ068i003p00937

Grewal, D.S., Dasgupta, R., Holmes, A.K., Costin, G., Li, Y., Tsuno, K., 2019a. The fate of nitrogen during core-mantle separation on Earth. Geochimica et Cosmochimica Acta 251, 87–115. https://doi.org/10.1016/j.gca.2019.02.009

Grewal, D.S., Dasgupta, R., Marty, B., 2021. A very early origin of isotopically distinct nitrogen in inner Solar System protoplanets. Nat Astron 5, 356–364. https://doi.org/10.1038/s41550-020-01283-y

Grewal, D.S., Dasgupta, R., Sun, C., Tsuno, K., Costin, G., 2019b. Delivery of carbon, nitrogen, and sulfur to the silicate Earth by a giant impact. Sci. Adv. 5, eaau3669. https://doi.org/10.1126/sciadv.aau3669

Grewal, D.S., Dasgupta, R., Sun, C., Tsuno, K., Costin, G., 2019c. Delivery of carbon, nitrogen, and sulfur to the silicate Earth by a giant impact. Sci. Adv. 5, eaau3669. https://doi.org/10.1126/sciadv.aau3669

Grewal, D.S., Sun, T., Aithala, S., Hough, T., Dasgupta, R., Yeung, L.Y., Schauble, E.A., 2022. Limited nitrogen isotopic fractionation during core-mantle differentiation in rocky protoplanets and planets. Geochimica et Cosmochimica Acta 338, 347–364. https://doi.org/10.1016/j.gca.2022.10.025

Halliday, A.N., 2013. The origins of volatiles in the terrestrial planets. Geochimica et Cosmochimica Acta 105, 146–171. https://doi.org/10.1016/j.gca.2012.11.015

Halliday, A.N., Wänke, H., Birck, J.-L., Clayton, R.N., 2001. The Accretion, Composition and Early Differentiation of Mars. Space Science Reviews 96, 197–230. https://doi.org/10.1023/A:1011997206080

Hellmann, J.L., Hopp, T., Burkhardt, C., Kleine, T., 2020. Origin of volatile element depletion among carbonaceous chondrites. Earth and Planetary Science Letters 549, 116508. https://doi.org/10.1016/j.epsl.2020.116508

Hirschmann, M.M., 2016. Constraints on the early delivery and fractionation of Earth's major volatiles from C/H, C/N, and C/S ratios. American Mineralogist 101, 540–553. https://doi.org/10.2138/am-2016-5452

Holzheid, A., Sylvester, P., O'Neill, H.S.C., Rubie, D.C., Palme, H., 2000. Evidence for a late chondritic veneer in the Earth's mantle from high-pressure partitioning of palladium and platinum. Nature 406, 396–399. https://doi.org/10.1038/35019050

Huang, D., Badro, J., 2018. Fe-Ni ideality during core formation on Earth. American Mineralogist 103, 1707–1710. https://doi.org/10.2138/am-2018-6651

Huang, D., Brodholt, J., Sossi, P., Li, Y., Murakami, M., 2022. Nitrogen Speciation in Silicate Melts at Mantle Conditions From Ab Initio Simulations. Geophysical Research Letters 49, e2021GL095546. https://doi.org/10.1029/2021GL095546

Huang, Dongyang, Murakami, M., Brodholt, J., McCammon, C., Petitgirard, S., 2022. Structural evolution in a pyrolitic magma ocean under mantle conditions. Earth and Planetary Science Letters 584, 117473. https://doi.org/10.1016/j.epsl.2022.117473

Huang, D., Siebert, J., Sossi, P., Kubik, E., Avice, G., Murakami, M., 2024. Nitrogen sequestration in the core at megabar pressure and implications for terrestrial accretion. Geochimica et Cosmochimica Acta. https://doi.org/10.1016/j.gca.2024.05.010

Jackson, C.R.M., Bennett, N.R., Du, Z., Cottrell, E., Fei, Y., 2018. Early episodes of high-pressure core formation preserved in plume mantle. Nature 553, 491–495. https://doi.org/10.1038/nature25446

Jackson, C.R.M., Cottrell, E., Du, Z., Bennett, N.R., Fei, Y., 2021. High pressure redistribution of nitrogen and sulfur during planetary stratification. Geochem. Persp. Let. 37–42. https://doi.org/10.7185/geochemlet.2122

Karki, B.B., Bhattarai, D., Mookherjee, M., Stixrude, L., 2010. Visualization-based analysis of structural and dynamical properties of simulated hydrous silicate melt. Phys Chem Minerals 37, 103–117. https://doi.org/10.1007/s00269-009-0315-1

Lammer, H., Kasting, J.F., Chassefière, E., Johnson, R.E., Kulikov, Y.N., Tian, F., n.d. Atmospheric Escape and Evolution of Terrestrial Planets and Satellites.

Lee, T., Papanastassiou, D.A., Wasserburg, G.J., 1976. Correction [to "Demonstration of 26Mg excess in Allende and evidence for 26Al"]. Geophysical Research Letters 3, 109–112. https://doi.org/10.1029/GL003i002p00109

Li, Y., Wiedenbeck, M., Monteleone, B., Dasgupta, R., Costin, G., Gao, Z., Lu, W., 2023. Nitrogen and carbon fractionation in planetary magma oceans and origin of the superchondritic C/N ratio in the bulk silicate Earth. Earth and Planetary Science Letters 605, 118032. https://doi.org/10.1016/j.epsl.2023.118032

Li, Y.-F., Marty, B., Shcheka, S., Zimmermann, L., Keppler, H., 2016. Nitrogen isotope fractionation during terrestrial core-mantle separation. Geochemical Perspectives Letters 2, 138–147. https://doi.org/10.7185/geochemlet.1614

Libourel, G., Marty, B., Humbert, F., 2003. Nitrogen solubility in basaltic melt. Part I. Effect of oxygen fugacity. Geochimica et Cosmochimica Acta 67, 4123–4135. https://doi.org/10.1016/S0016-7037(03)00259-X

Lodders, K., 2003. Solar System Abundances and Condensation Temperatures of the Elements. ApJ 591, 1220–1247. https://doi.org/10.1086/375492

Ma, Z., 2001. Thermodynamic description for concentrated metallic solutions using interaction parameters. Metall Mater Trans B 32, 87–103. https://doi.org/10.1007/s11663-001-0011-0

Maas, C., Manske, L., Wünnemann, K., Hansen, U., 2021. On the fate of impact-delivered metal in a terrestrial magma ocean. Earth and Planetary Science Letters 554, 116680. https://doi.org/10.1016/j.epsl.2020.116680

Mao, H.K., Bell, P.M., Shaner, J.W., Steinberg, D.J., 2008. Specific volume measurements of Cu, Mo, Pd, and Ag and calibration of the ruby R1 fluorescence pressure gauge from 0.06 to 1 Mbar. Journal of Applied Physics 49, 3276–3283. https://doi.org/10.1063/1.325277

Marty, B., 2012. The origins and concentrations of water, carbon, nitrogen and noble gases on Earth. Earth and Planetary Science Letters 313–314, 56–66. https://doi.org/10.1016/j.epsl.2011.10.040

Moynier, F., Day, J.M.D., Okui, W., Yokoyama, T., Bouvier, A., Walker, R.J., Podosek, F.A., 2012. PLANETARY-SCALE STRONTIUM ISOTOPIC HETEROGENEITY AND THE AGE OF VOLATILE DEPLETION OF EARLY SOLAR SYSTEM MATERIALS. ApJ 758, 45. https://doi.org/10.1088/0004-637X/758/1/45

Mysen, B.O., Tomita, T., Ohtani, E., Suzuki, A., 2014. Speciation of and D/H partitioning between fluids and melts in silicate-D-O-H-C-N systems determined in-situ at upper mantle temperatures, pressures, and redox conditions. American Mineralogist 99, 578–588. https://doi.org/10.2138/am.2014.4575

O'Neill, H.St.C., Eggins, S.M., 2002. The effect of melt composition on trace element partitioning: an experimental investigation of the activity coefficients of FeO, NiO, CoO, MoO2 and MoO3 in silicate melts. Chemical Geology 186, 151–181. https://doi.org/10.1016/S0009-2541(01)00414-4

Ono, S., Kikegawa, T., Hirao, N., Mibe, K., 2010. Letter. High-pressure magnetic transition in hcp-Fe. American Mineralogist 95, 880–883. https://doi.org/10.2138/am.2010.3430

Palme, H., Lodders, K., Jones, A., 2014. Solar System Abundances of the Elements. Planets, Asteriods, Comets and The Solar System, Volume 2 of Treatise on Geochemistry (Second Edition). Edited by Andrew M. Davis. Elsevier, 2014., p.15-36 2. https://doi.org/10.1016/B978-0-08-095975-7.00118-2

Prescher, C., Prakapenka, V.B., 2015. DIOPTAS: a program for reduction of two-dimensional X-ray diffraction data and data exploration. High Pressure Research 35, 223–230. https://doi.org/10.1080/08957959.2015.1059835

Qaddah, B., Monteux, J., Clesi, V., Bouhifd, M.A., Le Bars, M., 2019. Dynamics and stability of an iron drop falling in a magma ocean. Physics of the Earth and Planetary Interiors 289, 75–89. https://doi.org/10.1016/j.pepi.2019.02.006

Righter, K., Rowland Ii, R., Yang, S., Humayun, M., 2020. Activity coefficients of siderophile elements in Fe-Si liquids at high pressure. Geochem. Persp. Let. 44–49. https://doi.org/10.7185/geochemlet.2034

Roskosz, M., Bouhifd, M.A., Jephcoat, A.P., Marty, B., Mysen, B.O., 2013. Nitrogen solubility in molten metal and silicate at high pressure and temperature. Geochimica et Cosmochimica Acta 121, 15–28. https://doi.org/10.1016/j.gca.2013.07.007

Schlichting, H.E., Sari, R., Yalinewich, A., 2015. Atmospheric mass loss during planet formation: The importance of planetesimal impacts. Icarus 247, 81–94. https://doi.org/10.1016/j.icarus.2014.09.053

Sekiya, M., Nakazawa, K., Hayashi, C., 1980. Dissipation of the Primordial Terrestrial Atmosphere Due to Irradiation of the Solar EUV. Progress of Theoretical Physics 64, 1968–1985. https://doi.org/10.1143/PTP.64.1968

Sha, X., Cohen, R.E., 2010. First-principles thermal equation of state and thermoelasticity of hcp Fe at high pressures. Phys. Rev. B 81, 094105. https://doi.org/10.1103/PhysRevB.81.094105

Shen, G., Wang, Y., Dewaele, A., Wu, C., Fratanduono, D.E., Eggert, J., Klotz, S., Dziubek, K.F., Loubeyre, P., Fat'yanov, O.V., Asimow, P.D., Mashimo, T., Wentzcovitch, R.M.M., 2020. Toward an international practical pressure scale: A proposal for an IPPS ruby gauge (IPPS-Ruby2020). High Pressure Research 40, 299–314. https://doi.org/10.1080/08957959.2020.1791107

Shi, L., Lu, W., Kagoshima, T., Sano, Y., Gao, Z., Du, Z., Liu, Y., Fei, Y., Li, Y., 2022. Nitrogen isotope evidence for Earth's heterogeneous accretion of volatiles. Nat Commun 13, 4769. https://doi.org/10.1038/s41467-022-32516-5

Siebert, J., Badro, J., Antonangeli, D., Ryerson, F.J., 2012. Metal–silicate partitioning of Ni and Co in a deep magma ocean. Earth and Planetary Science Letters 321–322, 189–197. https://doi.org/10.1016/j.epsl.2012.01.013

Speelmanns, I.M., Schmidt, M.W., Liebske, C., 2019. The almost lithophile character of nitrogen during core formation. Earth and Planetary Science Letters 510, 186–197. https://doi.org/10.1016/j.epsl.2019.01.004

Tagawa, S., Sakamoto, N., Hirose, K., Yokoo, S., Hernlund, J., Ohishi, Y., Yurimoto, H., 2021. Experimental evidence for hydrogen incorporation into Earth's core. Nat Commun 12, 2588. https://doi.org/10.1038/s41467-021-22035-0

Tonks, W.B., Melosh, H.J., 1993. Magma ocean formation due to giant impacts. Journal of Geophysical Research: Planets 98, 5319–5333. https://doi.org/10.1029/92JE02726

Tucker, J.M., Mukhopadhyay, S., 2014. Evidence for multiple magma ocean outgassing and atmospheric loss episodes from mantle noble gases. Earth and Planetary Science Letters 393, 254–265. https://doi.org/10.1016/j.epsl.2014.02.050

Urey, H.C., 1955. THE COSMIC ABUNDANCES OF POTASSIUM, URANIUM, AND THORIUM AND THE HEAT BALANCES OF THE EARTH, THE MOON, AND MARS* [WWW Document]. https://doi.org/10.1073/pnas.41.3.127

Vollstaedt, H., Mezger, K., Alibert, Y., 2020. Carbonaceous Chondrites and the Condensation of Elements from the Solar Nebula. ApJ 897, 82. https://doi.org/10.3847/1538-4357/ab97b4

Walker, D., Agee, C., 1989. Partitioning "equilibrium", temperature gradients, and constraints on Earth differentiation. Earth and Planetary Science Letters 96, 49–60. https://doi.org/10.1016/0012-821X(89)90123-4

Wang, Z., Becker, H., 2013. Ratios of S, Se and Te in the silicate Earth require a volatile-rich late veneer. Nature 499, 328–331. https://doi.org/10.1038/nature12285

Wasson, J.T., Kallemeyn, G.W., Runcorn, S.K., Turner, G., Woolfson, M.M., 1997. Compositions of chondrites. Philosophical Transactions of the Royal Society of London. Series A, Mathematical and Physical Sciences 325, 535–544. https://doi.org/10.1098/rsta.1988.0066

Wetherill, G.W., 1985. Occurrence of Giant Impacts during the Growth of the Terrestrial Planets. Science 228, 877–879.

Wu, Z., Wentzcovitch, R.M., Umemoto, K., Li, B., Hirose, K., Zheng, J.-C., 2008. Pressure-volume-temperature relations in MgO: An ultrahigh pressure-temperature scale for planetary sciences applications. Journal of Geophysical Research: Solid Earth 113. https://doi.org/10.1029/2007JB005275

Experiment	**Sample Design**	**P (GPa)**	**P (GPa) ±**	**T (K)**	**T (K) ±**	**ΔIW**	**ΔIW ±**	**log $D_N^{m/s}$ (at)**
N28-3	MORB:FeN:MORB	38	7	2728	68	-1.91	0.03	1.026
N32-2	MORB:FeN:MORB	40	1	3395	79	-1.49	0.10	0.504
N49-1	MORB:FeN:MORB	63	2	4774	61	-1.57	0.11	0.400
N65-3	MORB:FeN:MORB	83	2	5171	60	-1.73	0.06	0.262
N39-1	MORB:FeN:MORB	52	3	4316	42	-1.87	0.01	0.404
N39-2	MORB:FeN:MORB	53	3	4845	73	-1.36	0.08	0.400
*NFO_2-2Fe-1	MORB:FeN:MORB	69	4	5038	22	-1.42	0.03	0.332
*NFO_2-2Fe-2	MORB:FeN:MORB	65	4	3434	187	-1.95	0.03	0.402
*NFO_2-4Fe-1	MORB:FeN:MORB	67	2	5120	163	-1.68	0.15	0.310
**NMO50-3	MgO:2Silicate+1FeN :MgO	68	1	5275	61	-1.24	0.06	0.608
**NMO30-2	MgO:2Silicate+1FeN :MgO	43	1	4066	420	-1.03	0.02	1.002
N75-1	MORB:FeN:MORB	86	2	5365	295	-1.42	0.04	0.277
N85-3	MORB:FeN:MORB	103	2	5609	202	-1.15	0.07	0.234
*NFO_2-1Fe-1	MORB:FeN:MORB	60	2	4937	460	-1.63	0.10	0.223
*NFO_2-1Fe-2	MORB:FeN:MORB	60	2	4868	93	-1.54	0.02	0.305
**NMO50-1	MgO:2Silicate+1FeN :MgO	67	1	4717	140	-1.05	0.02	0.788
N-MA-15-1	2MORB+1FeN	15	0.5	2773	20	-2.51	0.06	1.193

Table 1: Experimental conditions. The MORB:Fe_xN:MORB sample design represents our nominal compositional design used for the pressure series and the MgO:2Silicate+1Fe_xN:MgO design represents our MgO saturated compositional design. The N-MA-15-1 experiment is the multi-anvil experiment. *Reported pressure was measured using diamond edge Raman spectroscopy and represents the average pressure in the sample chamber after heating and includes thermal pressure. Pressure uncertainties are the standard deviation of pressure measurements across the sample chamber. The temperature measurements are average values of multiple spectra collected in succession with reported uncertainties as their standard deviation. ΔIW was calculated using methods in section 3.3. Error on ΔIW was computed by propagating analytical uncertainties for FeO and Fe.* $D_N^{m/s}$ *is the partition coefficient of nitrogen calculated from analytical measurements in mole fraction. (*) Experiments designed with variable FeO content in starting composition to explore the effect of oxygen fugacity. (**) MgO-saturated DAC experiments.*

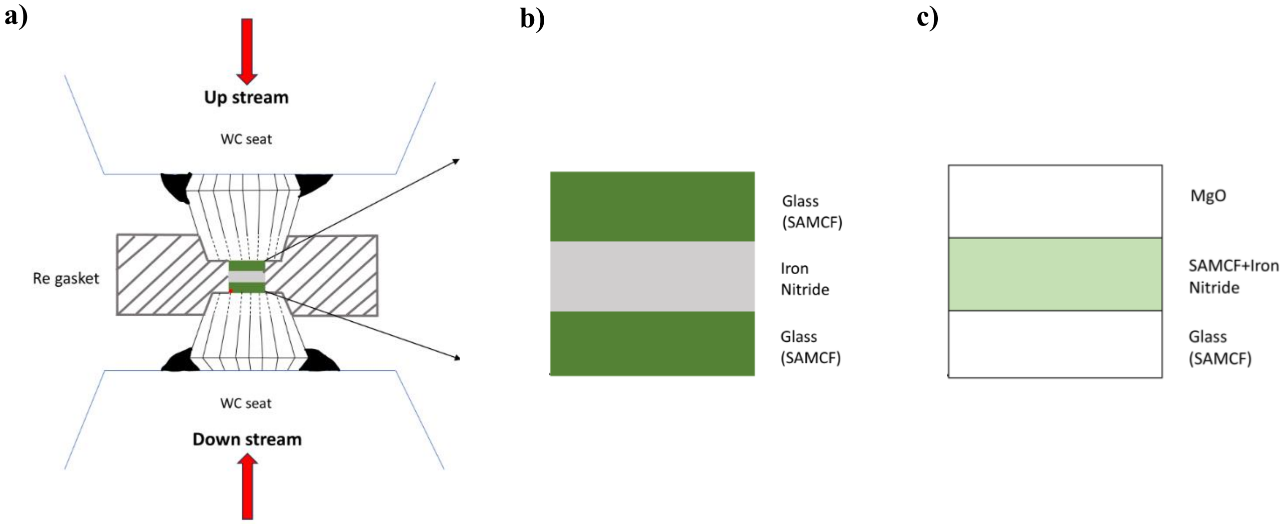

Figure 1 a) Schematic of an assembled diamond anvil cell. *Red arrows: IR laser beam direction.* Layered stacking of starting compositions for **b) Nominal design, c) MgO saturated design**. *SAMCF depicts the components* SiO_2*,* Al_2O_3*, MgO, CaO, and FeO in the glass/silicate starting composition*.

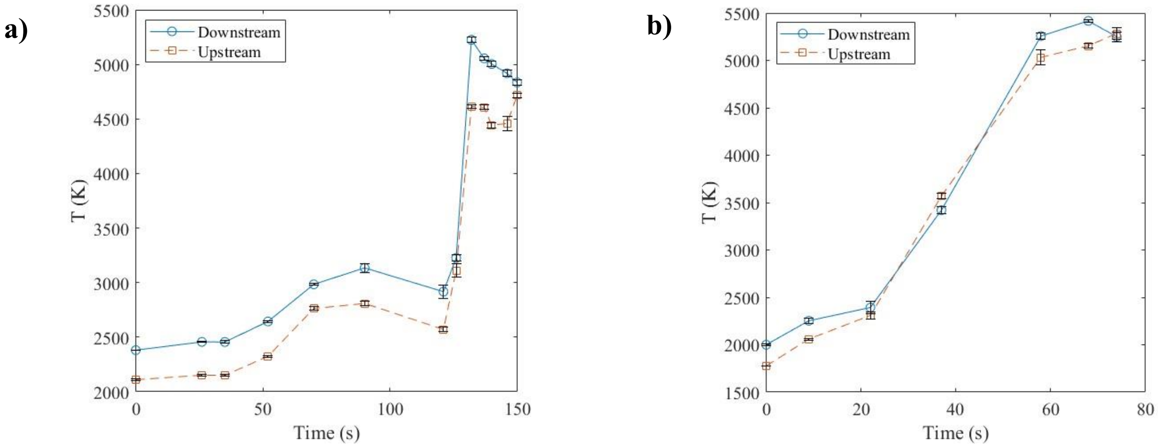

Figure 2: Time-Temperature paths of experiments a) N49-1 and b) NMO50-3. The upstream and downstream temperatures were monitored throughout the run duration of the experiment. Error bars are standard deviations on the number of T-measurements acquired at each time increment (x-axis) from the beginning of laser heating the sample marked at 0 s.

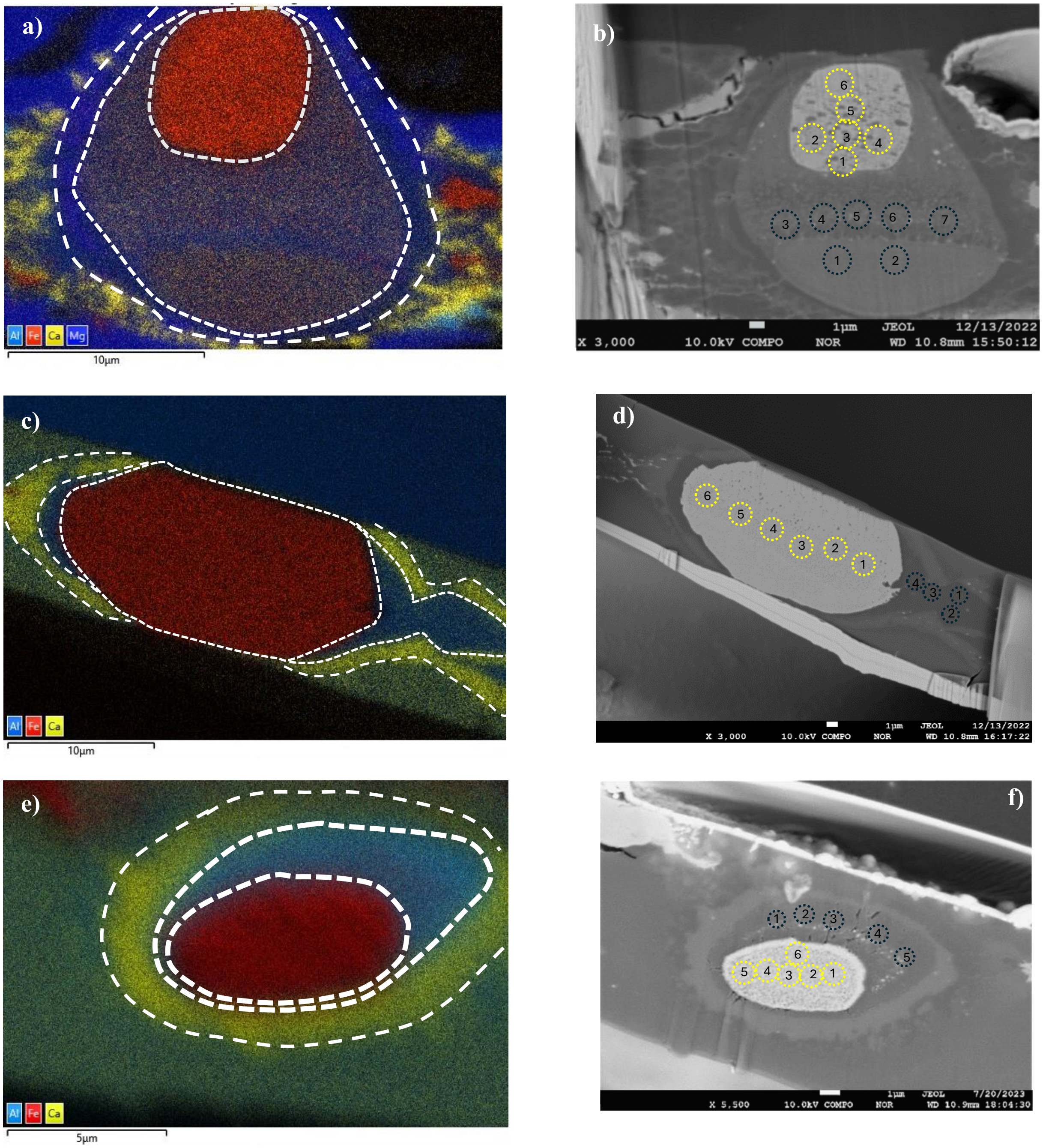

Figure 3: SE images showing cross-sections of heated spots. a) NMO50-3: [MgO-(Fe$_{2\text{-}4}$N+glass)-MgO] designed experiment run at 69 GPa, 5794 K showing MgSiO$_3$ crystallization (deep blue) around metal (red/brown)-silicate phases (light blue). **b) Compositional image for NMO50-3 c) N49-1:[glass-Fe$_{2\text{-}4}$N-glass] or nominal designed experiment** run at 63 GPa, 5013 K showing CaSiO$_3$ crystallization (yellow) around the metal-silicate phases. **d) Compositional image for (c)**. **e) N85-3: [glass-Fe$_{2\text{-}4}$N-glass]** run at 103 GPa, 5609 K. **f) Compositional image for (e).** Dashed blue circles are WDS measurement spots in silicate phase. Dashed yellow circles are WDS measurement spots in metallic phase. Analytical values tabulated in Table S-2 and S-3 show average values of multiple measurements on the metallic or the silicate phase as shown in these figures, along with their standard deviations, for each heated spot.

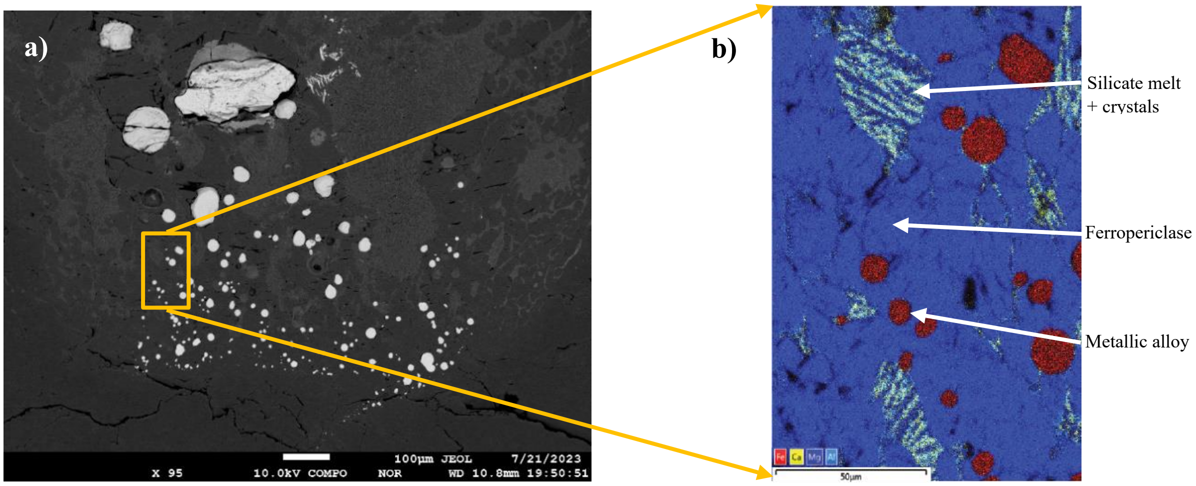

Figure 4: a) BSE image of multi-anvil experiment run at 15 GPa and 2773 K. b) zoomed in EDS map of a region within the experiment showing distribution of metallic alloy (red), silicate melt and clusters of elongated MgO, (Mg,Ca)SiO$_3$ crystals, and ferropericlase groundmass (blue).

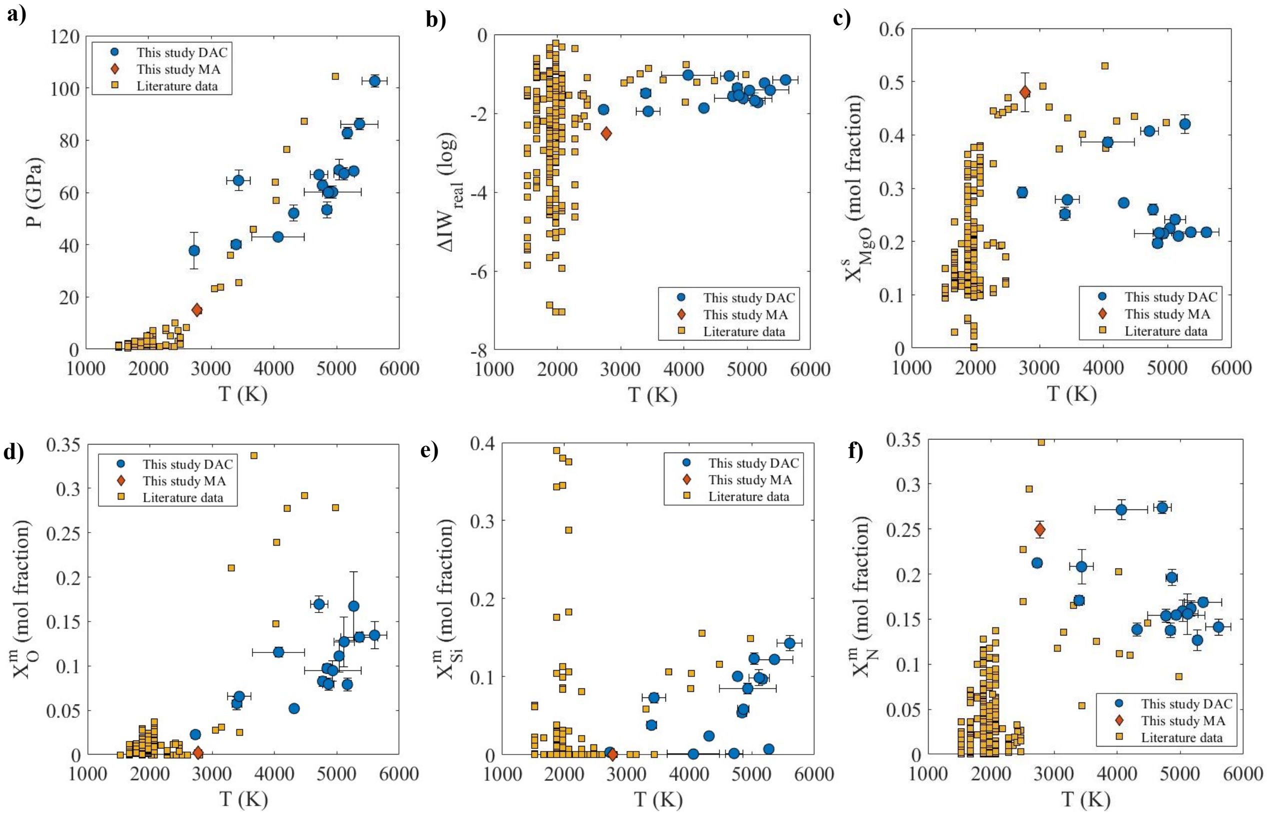

Figure 5 PTX distribution of experimental data for nitrogen partitioning between metal and silicate. a) pressure-temperature distribution, **b)** oxygen fugacity vs temperature distribution, **c)** MgO content of silicate melt (melt chemistry distribution), **d)** O content in the metal, **e)** Si content in the metal. **f)** N content in the metal. Error bars for our data are analytical uncertainties calculated as 1-sigma around mean.

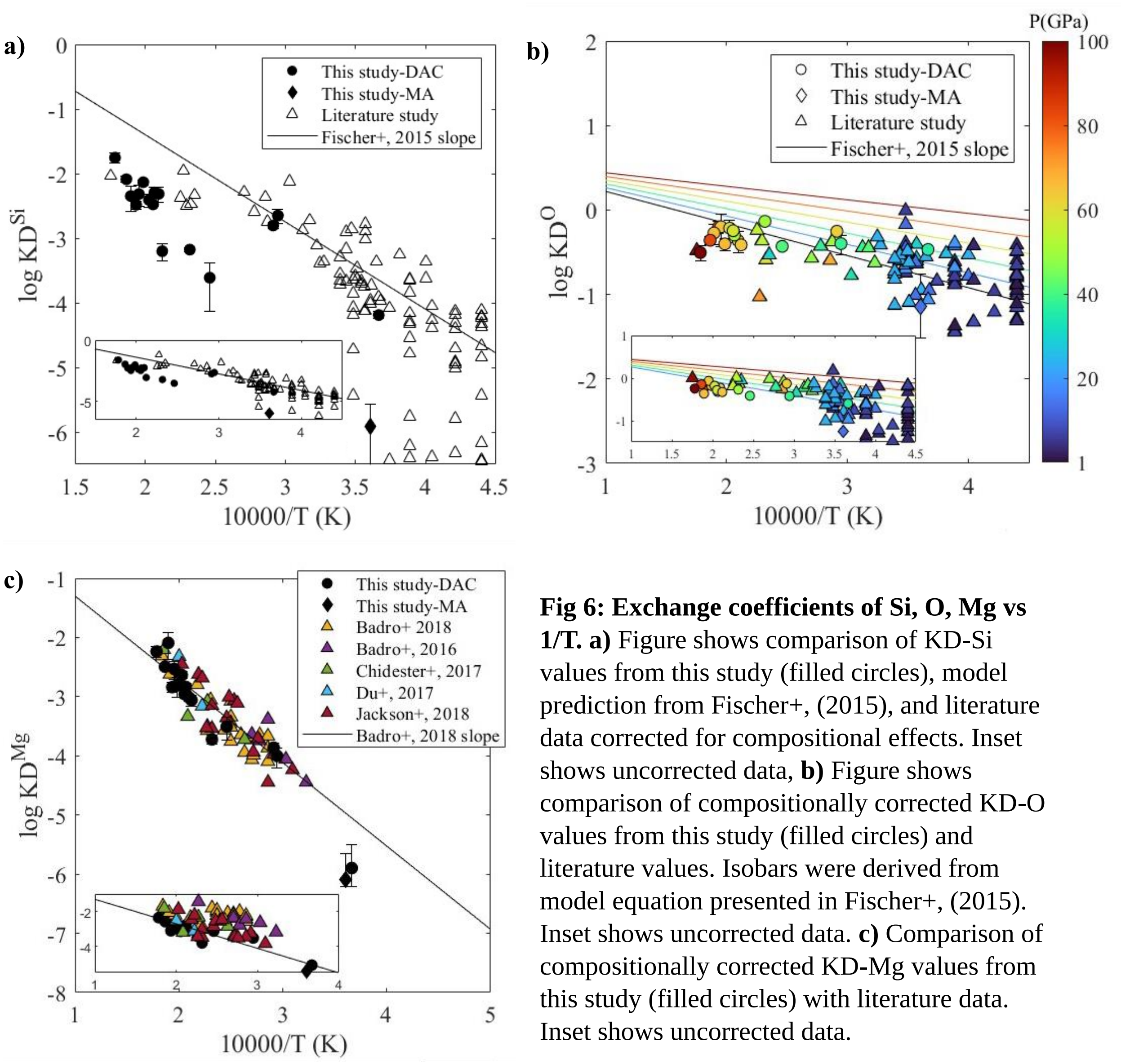

Fig 6: Exchange coefficients of Si, O, Mg vs 1/T. a) Figure shows comparison of KD-Si values from this study (filled circles), model prediction from Fischer+, (2015), and literature data corrected for compositional effects. Inset shows uncorrected data, **b)** Figure shows comparison of compositionally corrected KD-O values from this study (filled circles) and literature values. Isobars were derived from model equation presented in Fischer+, (2015). Inset shows uncorrected data. **c)** Comparison of compositionally corrected KD-Mg values from this study (filled circles) with literature data. Inset shows uncorrected data.

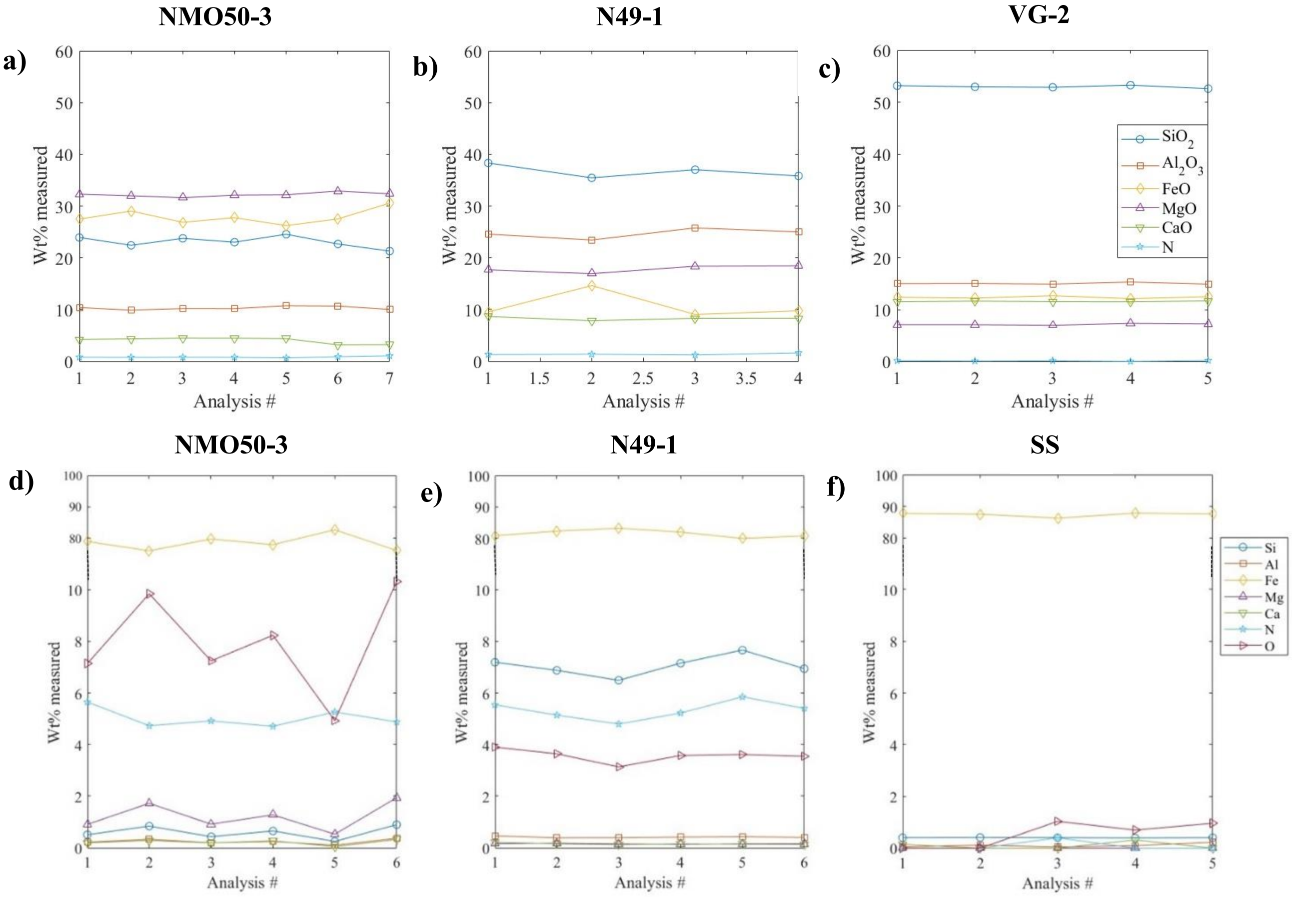

Figure 7: Microprobe (WDS) measurements across silicate a) NMO50-3, b) N49-1, c) volcanic glass (VG-2) **and metallic domains** d) NMO50-3, e) N49-1, f) stainless steel (SS). NMO50-3 represents the MgO saturated experiments and N49-1 represents analysis of a nominal experimental design. Analysis numbers represent individual spots within the domains in Fig 3. Volcanic glass and stainless steel are secondary standards used.

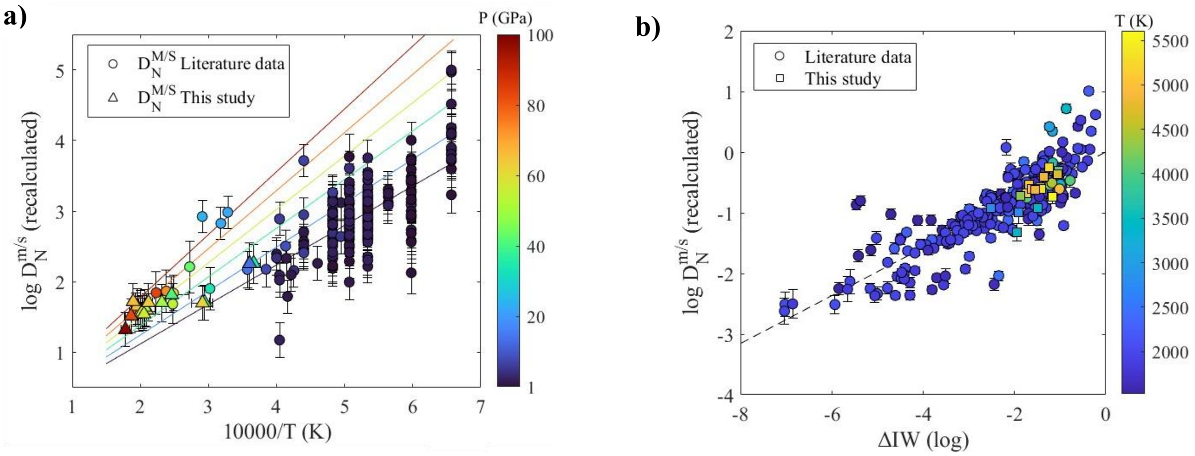

Figure 8: a) Effect of pressure and temperature on $D_N^{m/s}$. Partition coefficients are recalculated for compositional effects using our model. The isobars are our model predictions of $D_N^{m/s}$ considering the effects of pressure and temperature. Data on y-axis are recalculated to zero compositional effects and to IW. **b) Effect of oxygen fugacity on $D_N^{m/s}$.** Partition coefficients on y-axis are recalculated for the effect of P, T, and compositional effects other than oxygen fugacity using our model. Data points are color coded for the P or T they were acquired at. Error bars represent absolute uncertainties calculated from analytical uncertainties and recalculation assuming a normal distribution.

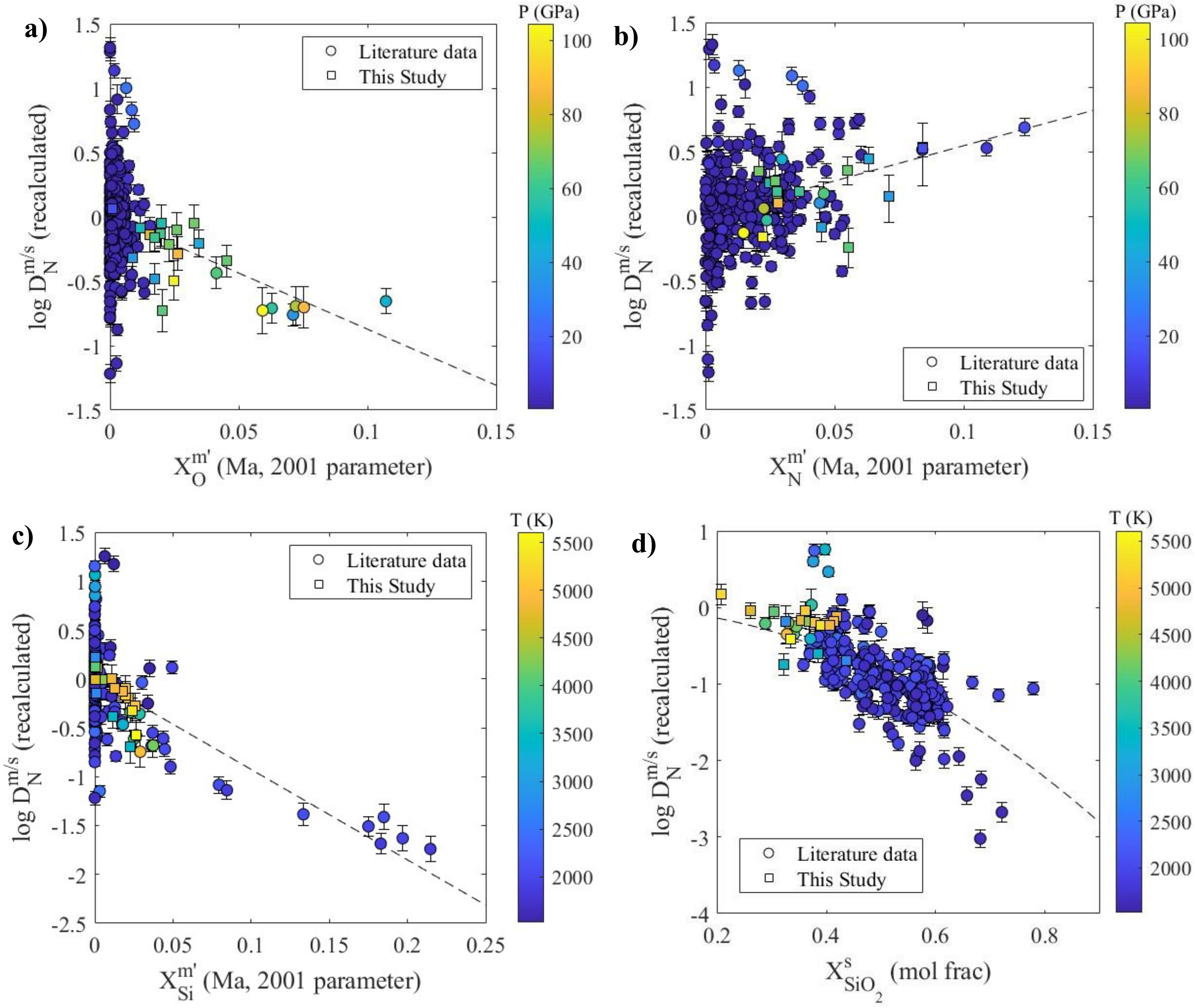

Figure 9: Effect of alloy and silicate chemistry on $D_N^{m/s}$. a) Si content and **b)** O content in the metallic alloy make nitrogen less siderophile. **c)** N enrichment in the alloy makes nitrogen more siderophile. **d)** SiO_2 enrichment in the silicate makes nitrogen less siderophile. X-axis represents alloy parameters of N, O and Si calculated using the Ma, (2001) approach considering the N-N, N-O and Si-N interactions. Data on y-axis are recalculated to no PTX effects and to IW except for the parameter on the respective x-axis in their functional form. Data points are color coded for the P or T they were acquired at. Error bars represent absolute uncertainties calculated from analytical uncertainties and compositional recalculation assuming a normal distribution.

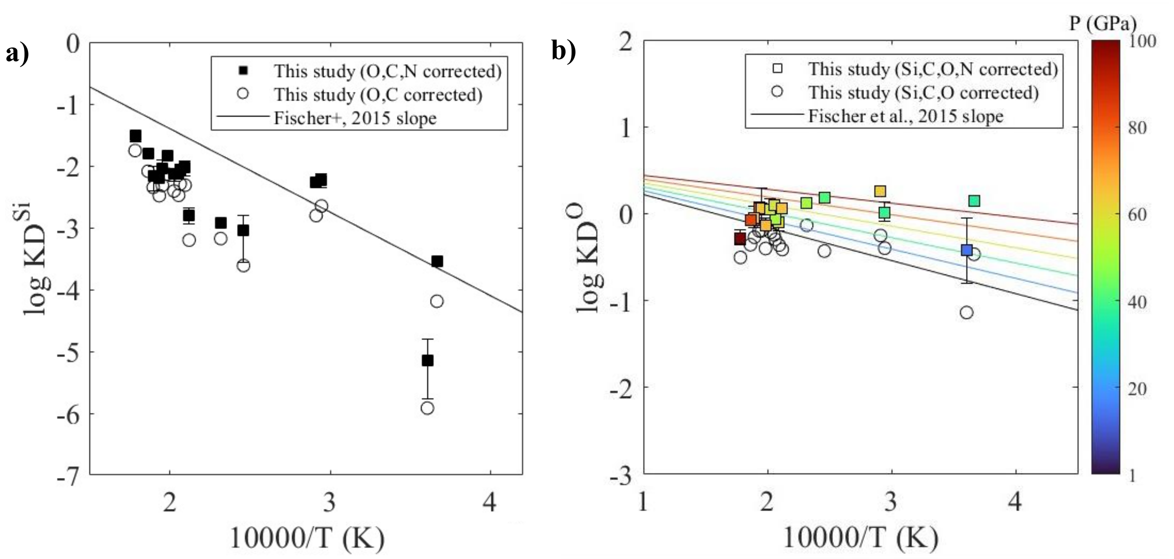

Figure 10: a) KD_{Si} recalculated for N-Si interaction. b) KD_O recalculated for N-O interaction. ε_N^O and ε_{Si}^O values were based on our model fits in Eq 7. Error bars are absolute uncertainties calculated from analytical uncertainties.

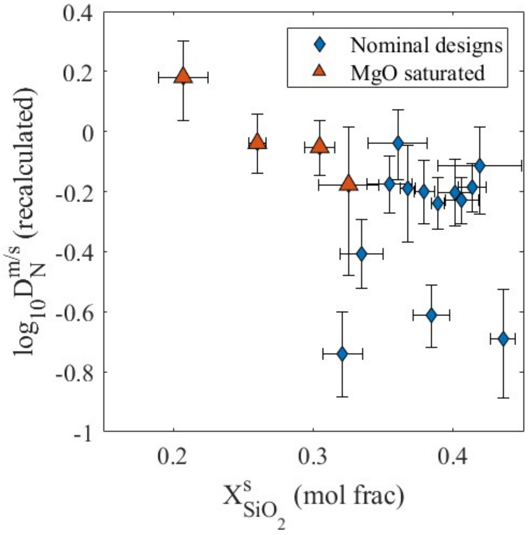

Figure 11: Effect of melt composition on D_N across different experimental designs. Partition coefficients are recalculated to IW and for no P, T, X effects except for the effect of SiO_2. Error bars on x-axis represent analytical uncertainty. Vertical error bars are calculated by propagating analytical uncertainties through PTX recalculations based on Eq 7.

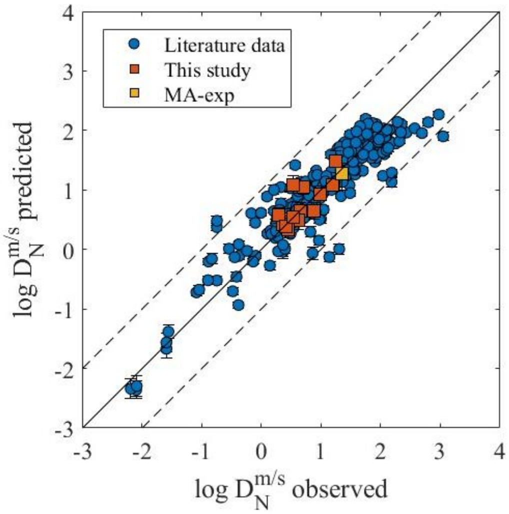

Figure 12: 1:1 comparison of Model based D_N predictions from eq 7 on y-axis with the measured (observed) $D_N^{m/s}$ values on the x-axis. The R^2 of the regression is 0.85. MA-exp is the multi-anvil data that was not included in our model formulation of Eq 7.

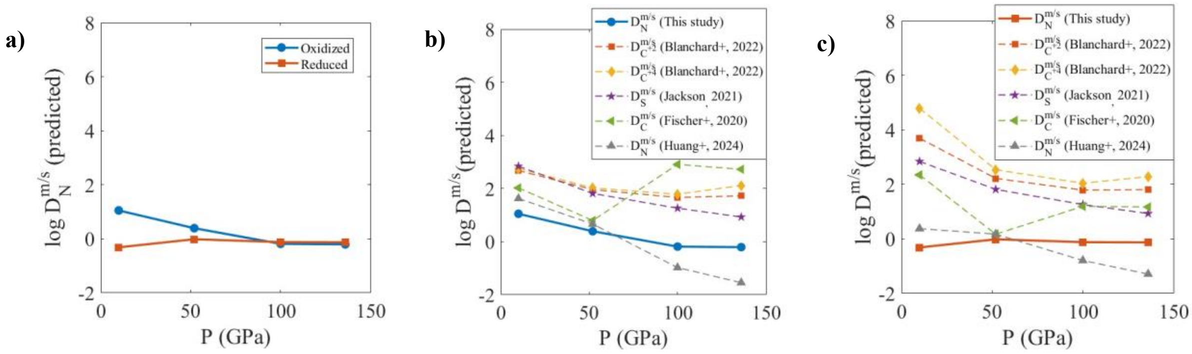

Figure 13 a) Application of nitrogen partitioning model to core formation for an oxidized system and a reduced system. **Partition coefficients of N, C, H, and S across core formation PT conditions for b) oxidized protoplanet scenarios c) reduced protoplanet scenarios.**

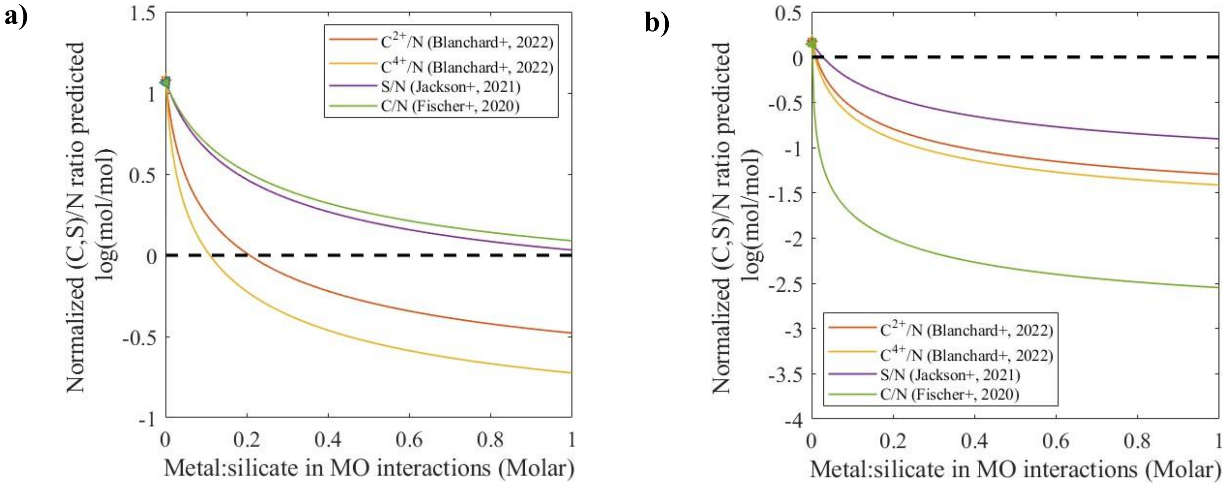

Figure 14 a) "Reduced" impact scenario, b) "Oxidized" impact scenario. C/N and S/N ratios in magma ocean (MO) environments when the smaller impactor core (equilibrated at 10 GPa, 2500 K) disintegrates and interacts with the MO under extreme PT conditions (100 GPa, 5000 K). X-axis shows the extent to which the impactor core gets diluted within the MO. Y-axis shows the S/N and the C/N ratio set in the magma ocean due to the metal-silicate interactions normalized to the bulk initial elemental ratios of the first step (see main text). Ratios above solid dashed line are elevated in C/N and S/N. Symbols at zero x-axis value are impactor core elemental ratios calculated from first step (see main text).

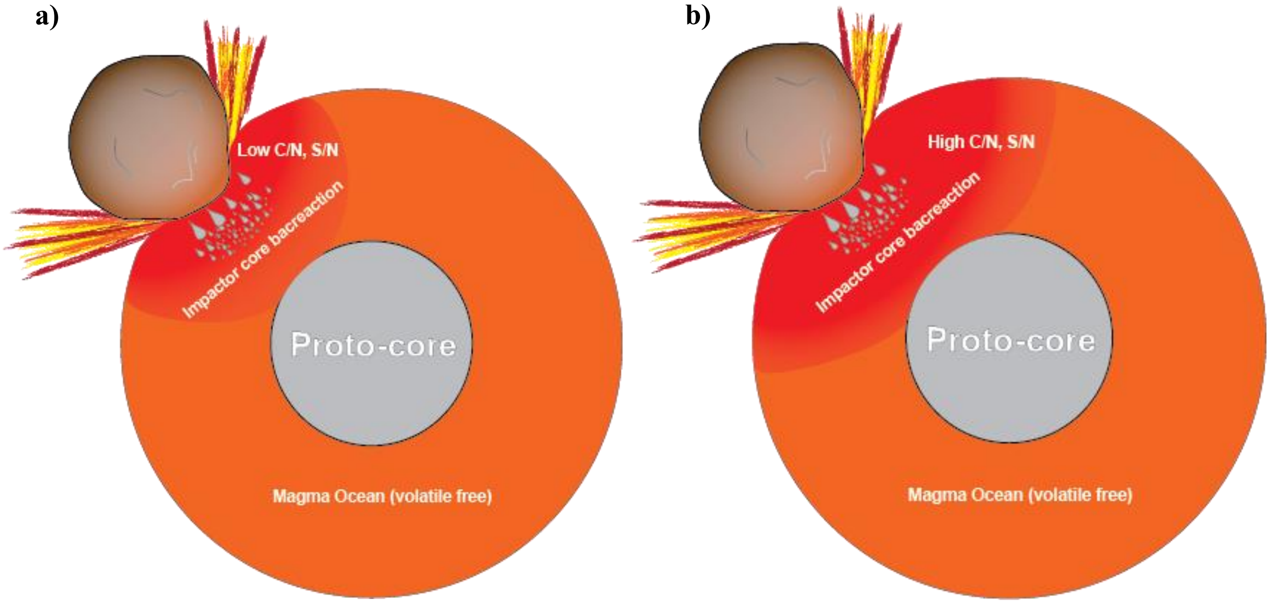

Figure 15 Schematic illustrating *second stage* of core formation model: The impactor core (gray drops) backreacts with the portion of the magma ocean it entrains (red domains within the MO). We model how VSEs are redistributed between metal and silicate, following their partitioning and the metal/silicate ratio of the reacting mass of impactor core and magma ocean. **a) shows a lower and b) shows a higher fraction of silicate mass entrained by the downwelling core of an impactor. A greater extent of metal dilution as in b) can produce elevated C/N and S/N ratios.**

Appendix A. Supplementary materials

Supplementary Tables

Table S-1: Temperature estimates for upstream (US) and downstream (DS) sides of DACs for each data point. T-rax files can be used to reproduce temperature estimates using the pixel ranges and wavelengths used to select ROI on light spectra captured on CCD.

N39-2	**N28-3**	**N49-1**	**N49-2**	**N32-2**	**N75-1**	**N85-3**	**NFO_2-1Fe-1**	**NFO_2-1Fe-2**
J8	J21	J2	J2	J9	F18	F6	F11	F11
18-36	38 to 44	1 to 13	16 to 21	21 to 36	1 to 35	54 to 78	2 to 12	13-30
35	43	13	21	35	35	77	10	29
4783	2771	4716	4342	3472	5073	5410	4467	4788
49	23	19	11	13	46	45	38	54
663-777	662-777	665-774	663-776	662-784	663-777	663-777	662-771	663-778
80-86	82-87	80-86	80-86	81-86	81-85	81-85	81-85	81-85
4907	2686	4832	4282	3318	5658	5808	5396	4951
21	72	20	123	24	20	18	16	31
660-778	662-778	661-778	661-779	661-780	662-779	661-779	660-779	672-781
130-136	131-136	131-136	131-136	131-136	130-136	131-136	130-137	131-136
4845	2728	4774	4312	3395	5365	5609	4937	4868
73	68	61	93	79	295	202	460	93

Sample name	**NFO_2-4Fe-1**	**NFO_2-2Fe-1**	**NFO_2-2Fe-2**	**N65-3**	**NMO50-1**	**NMO50-3**	**NMO30-2**	**N39-1**
Trax file name	O8	O3	O3	O17	O27	O27	O10	J8
Trax file range for hotspot (.spe)	1 to 8	11 to 19	20 to 30	21 to 26	1 to 10	21 to 30	15 to 23	1 to 16
Trax file used for temperature determination (.spe)	7	18	30	26	10	29	23	16
US (K)	4936	5022	3249	5117	4851	5300	4484	4295
± (K)	19	10	33	27	20	61	54	30
US wavelength (nm)	662-775	661-779	662-778	661-780	661-779	662-780	663-779	662-779
US pixel range	81-85	130-137	72-98	81-85	80-87	80-84	80-86	81-88
DS (K)	5282	5054	3619	5226	4579	5250	3648	4337
± (K)	17	18	19	22	25	50	30	41
DS wavelength (nm)	662-779	661-780	661-780	662-779	661-779	661-779	662-779	661-779
DS pixel range	130-135	130-137	131-136	129-135	130-136	130-135	131-135	129-136
mean T (using mid US and DS)	5120	5038	3434	5171	4717	5275	4066	4316
± (K)	163	22	187	60	140	61	420	42

Table S-2: Silicate analysis of our experimental data used for the formulation of Eq 7

N28-3	**N32-2**	**N49-1**	**N65-3**	**N39-1**	**N39-2**	**NFO_2-2Fe-1**	**NFO_2-2Fe-2**	**NFO_2-4Fe-1**	**NMO50-3**	**NMO30-2**	**N75-1**	**N85-3**	**NFO_2-1Fe-1**
5	6	5	6	3	8	8	4	12	7	11	4	4	5
47.45	41.29	36.76	42.88	39.35	43.35	39.48	34.27	38.40	24.29	34.54	39.30	33.99	43.76
0.41	1.26	1.59	1.53	0.46	2.97	0.74	0.67	2.39	1.63	0.94	0.36	0.79	1.35
16.10	18.67	25.06	25.47	24.31	20.29	24.76	29.10	23.99	10.84	8.62	28.87	28.70	22.77
0.21	0.96	0.50	1.26	0.60	0.79	0.16	1.55	1.23	0.75	0.22	0.76	0.73	0.88
8.02	12.55	10.22	7.96	7.95	14.39	11.51	6.65	9.49	26.79	21.33	11.08	14.58	9.65
0.40	2.89	3.02	1.02	0.35	2.45	0.64	0.57	3.29	3.19	0.70	1.09	2.54	2.17
21.34	18.11	18.07	15.06	19.54	13.65	15.71	19.95	17.24	33.10	29.37	14.73	14.81	15.25
0.74	0.68	0.25	0.45	0.18	0.30	0.18	0.59	0.52	1.49	0.34	0.54	0.42	0.49
6.57	8.03	8.41	6.42	7.48	6.99	6.75	7.97	8.97	4.12	5.44	3.90	5.96	6.28
0.20	0.61	0.26	0.13	0.22	0.35	0.11	1.32	1.54	0.48	0.12	0.21	0.21	0.27
0.51	1.34	1.48	2.21	1.37	1.33	1.80	2.06	1.90	0.86	0.72	2.11	1.96	2.29
0.12	0.22	0.15	0.18	0.39	0.37	0.24	0.09	0.27	0.16	0.07	0.04	0.15	0.19
100.00	100.00	100.00	100.00	100.00	100.00	100.00	100.00	100.00	100.00	100.00	100.00	100.00	100.00

Sample name	N-MA-15-1	NMO 50-1	NFO_2-1Fe-2
n	10	6	4
SiO2	39.00	28.92	43.06
±	1.81	0.55	1.05
Al2O3	8.65	10.85	22.62
±	0.86	0.18	0.29
FeO	4.37	24.44	10.16
±	0.61	0.84	0.49
MgO	38.69	30.37	15.38
±	3.53	0.52	0.25
CaO	8.85	4.45	6.37
±	1.51	0.08	0.15
N	0.45	0.97	2.41
±	0.17	0.12	0.10
Total	100.00	100.00	100.00

* Analysis and uncertainties are in wt%.

Table S-3: Metal analysis of our experimental data used for the formulation of Eq 7

NFO_2-2Fe-2	NFO_2-2Fe-	N39-2	N39-1	N65-3	N49-1	N32-2	N28-3
4	6	6	6	5	6	6	6
82.37	78.18	82.20	87.31	78.53	81.59	86.40	89.80
1.78	2.18	0.29	0.56	1.88	1.06	2.99	0.62
0.06	0.04	0.06	0.05	0.07	0.02	0.08	0.04
0.11	0.02	0.07	0.06	0.07	0.03	0.08	0.08
7.34	5.75	4.99	4.71	6.04	5.36	5.79	6.95
0.71	0.42	0.33	0.25	0.04	0.37	0.07	0.08
1.73	1.59	4.20	4.04	3.96	1.96	2.60	2.04
0.43	0.43	0.33	0.25	1.17	0.51	0.35	0.39
5.19	8.97	3.94	1.65	7.29	7.06	2.59	0.21
0.43	0.55	0.11	0.08	0.53	0.39	0.15	0.02
0.12	0.18	0.14	0.05	0.13	0.15	0.08	0.01
0.02	0.06	0.02	0.01	0.02	0.01	0.02	0.01
0.33	0.52	0.30	0.10	0.41	0.41	0.12	0.02
0.02	0.18	0.02	0.01	0.04	0.03	0.02	0.01
0.22	0.19	0.15	0.06	0.20	0.15	0.12	0.08
0.03	0.03	0.02	0.01	0.04	0.03	0.02	0.03
2.64	4.59	4.03	2.02	3.37	3.29	2.23	0.85
0.08	0.80	0.20	0.08	0.27	0.25	0.32	0.06
100.00	100.0	100.00	100.00	100.00	100.00	100.0	100.00

Exp Samples	**N-MA-15-1**	**NMO 50-1**	**NFO_2 -1Fe-2**	**NFO_2 -1Fe-1**	**N85-3**	**N75-1**	**NMO3 0-2**	**NMO5 0-3**	**NFO_2 -4Fe-1**
n	9	4	5	5	6	4	4	6	4
Fe	90.15	79.90	79.55	78.95	74.70	75.02	81.11	78.72	76.47
±	0.42	0.72	0.34	1.45	2.42	0.68	1.95	3.73	1.93
Ni	0.05	0.09	0.07	0.03	0.11	0.05	0.04	0.05	0.03
±	0.06	0.10	0.10	0.04	0.11	0.07	0.04	0.06	0.04
N	8.15	8.97	7.47	5.76	5.23	6.42	10.55	5.07	5.92
±	0.42	0.29	0.33	0.14	0.27	0.27	0.44	0.47	1.11
C	1.47	2.84	4.36	3.84	1.41	2.07	2.85	6.27	3.10
±	0.20	0.47	0.53	0.67	0.55	0.60	0.11	0.49	0.32
Si	0.01	0.14	4.48	6.37	10.65	9.35	0.08	0.59	7.58
±	0.02	0.04	0.15	0.51	0.67	0.23	0.06	0.23	1.17
Mg	0.04	0.28	0.13	0.25	0.45	0.28	0.17	1.21	0.32
±	0.04	0.05	0.01	0.01	0.07	0.02	0.07	0.49	0.08
Al	0.00	0.06	0.33	0.56	1.31	0.86	0.02	0.24	0.81
±	0.00	0.02	0.04	0.04	0.10	0.04	0.02	0.09	0.25
Ca	0.03	0.10	0.15	0.22	0.43	0.21	0.06	0.22	0.24
±	0.03	0.02	0.01	0.02	0.02	0.02	0.01	0.09	0.03
O	0.09	7.61	3.46	4.03	5.69	5.75	5.12	7.64	5.52
±	0.13	0.05	0.28	0.47	0.58	0.30	0.25	1.78	1.60
Total	100.00	100.0	100.00	100.00	100.00	100.00	100.00	100.00	100.00

* Analysis and uncertainties are in wt%.

Supplementary Figures

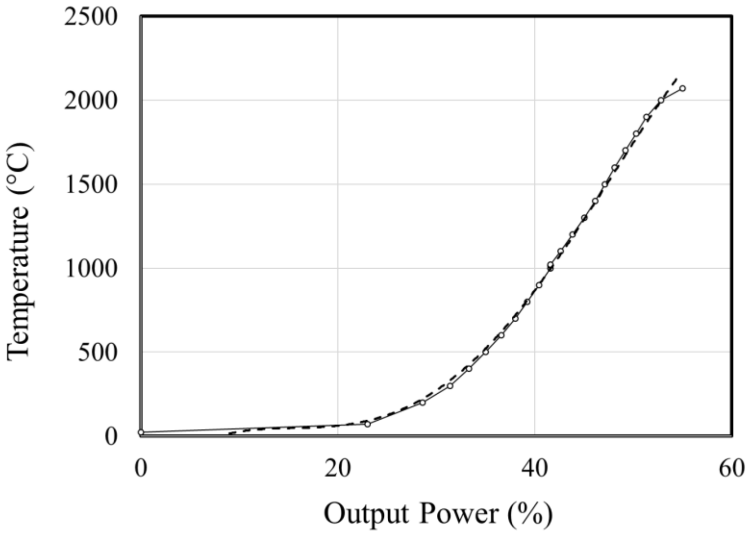

Fig S-1: Multi anvil power temperature curve. The solid curve corresponds to heating of our MA experiment. Beyond 2273 K thermocouples do not report true temperature due to contamination. Temperatures beyond 2273 K were inferred from previously run power-temperature curves (thick dashed lines)

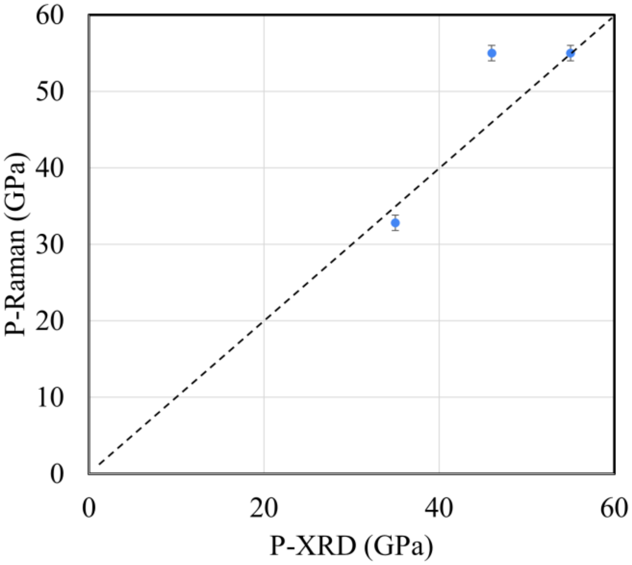

Fig S-2: Comparison of pressures measured using diamond edge Raman spectroscopy with pressures measured on the heated spots using synchrotron XRD measurements of MgO peaks. XRD based pressures estimates could be determined for MgO saturated experiments for which MgO peaks post experiments could be measured, and pressures evaluated using existing equation of states for MgO. The nominal designs did not have a pure phase for which EOS has been defined to evaluate its pressure and are not reported in this comparison. The dashed line represents a 1:1 correlation of pressures for both methods. Y-error bars are standard deviations on pressure based on Raman measurements acquired from 5 points across the sample chamber post heating.

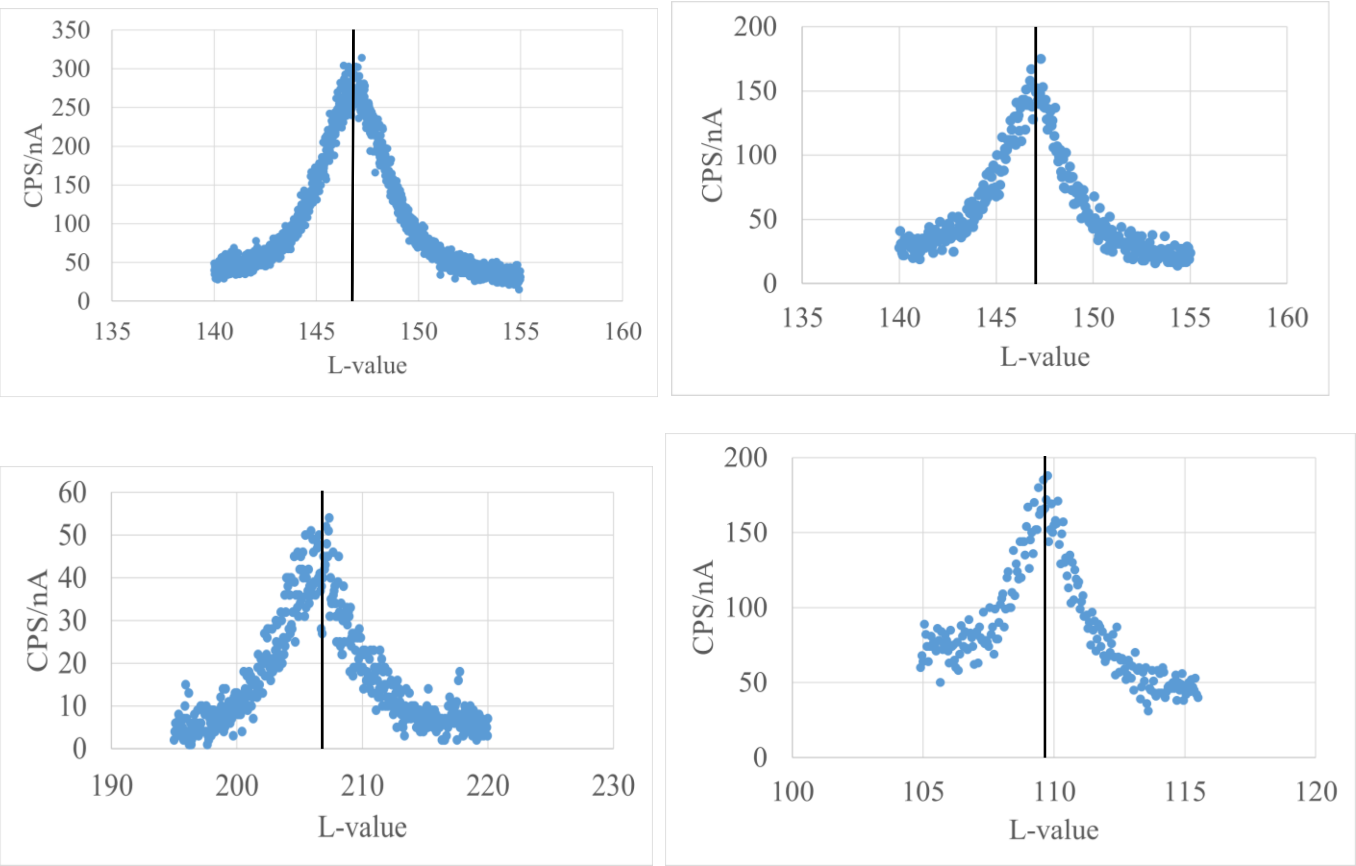

Fig S-3: Wave scans of **a) nitrogen in silicate** and **b) nitrogen c) carbon d) oxygen in metallic alloys** showing peak positions (L-value) for N, C, and O which were used to measure their concentrations. These wave scans were determined on our DAC samples. *Black solid line in the plots above denotes the peak position (x-axis) for each element.*

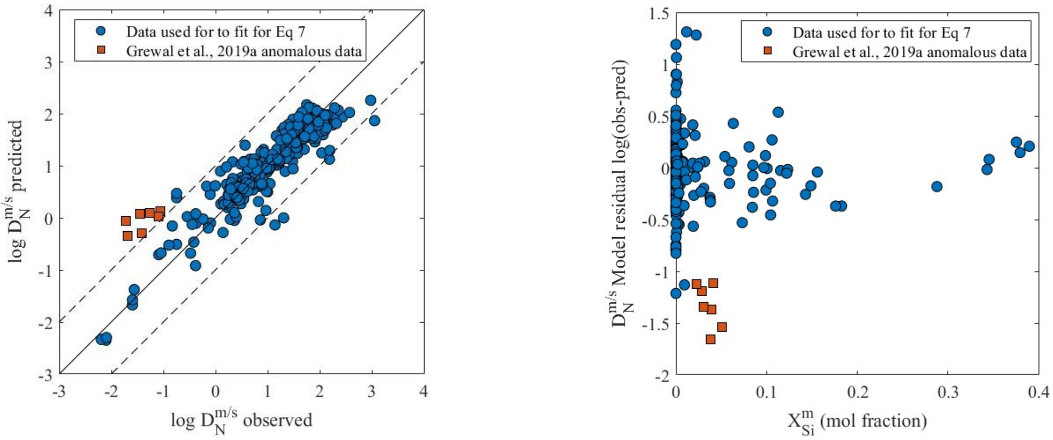

Fig S-4: a) Comparison of predicted vs observed $D_N^{m/s}$, b) Model residual vs Si content of metal We do not include 7 data points from Grewal et al., 2019a highlighted above. These data show systematic offset of D values from our model predictions that correlate with higher Si content in the metal. This systematic offset is not found in other Si bearing high PT and low PT experiments used in our compilation.